*Astronomy & Astrophysics* manuscript no. output
May 22, 2024


# *Euclid*: Early Release Observations – The intracluster light and intracluster globular clusters of the Perseus cluster★

M. Kluge[1], N. A. Hatch[★★2], M. Montes[3,4], J. B. Golden-Marx[2], A. H. Gonzalez[5], J.-C. Cuillandre[6], M. Bolzonella[7], A. Lançon[8], R. Laureijs[9], T. Saifollahi[8,10], M. Schirmer[11], C. Stone[12], A. Boselli[13,14], M. Cantiello[15], J. G. Sorce[16,17,18], F. R. Marleau[19], P.-A. Duc[20], E. Sola[21], M. Urbano[8], S. L. Ahad[22,23], Y. M. Bahé[24], S. P. Bamford[2], C. Bellhouse[2], F. Buitrago[25,26], P. Dimauro[27,28], F. Durret[29], A. Ellien[30], Y. Jimenez-Teja[31,28], E. Slezak[32], N. Aghanim[17], B. Altieri[33], S. Andreon[34], N. Auricchio[7], M. Baldi[35,7,36], A. Balestra[37], S. Bardelli[7], R. Bender[1,38], D. Bonino[39], E. Branchini[40,41,34], M. Brescia[42,43,44], J. Brinchmann[45,46], S. Camera[47,48,39], G. P. Candini[49], V. Capobianco[39], C. Carbone[50], J. Carretero[51,52], S. Casas[53], M. Castellano[27], S. Cavuoti[43,44], A. Cimatti[54], G. Congedo[55], C. J. Conselice[56], L. Conversi[57,33], Y. Copin[58], F. Courbin[24], H. M. Courtois[59], M. Cropper[49], A. Da Silva[60,61], H. Degaudenzi[62], J. Dinis[60,61], C. A. J. Duncan[56,63], X. Dupac[33], S. Dusini[64], M. Farina[65], S. Farrens[6], S. Ferriol[58], P. Fosalba[66,67], M. Frailis[68], E. Franceschi[7], M. Fumana[50], S. Galeotta[68], B. Garilli[50], W. Gillard[69], B. Gillis[55], C. Giocoli[7,70], P. Gómez-Alvarez[71,33], B. R. Granett[34], A. Grazian[37], F. Grupp[1,38], L. Guzzo[72,34], S. V. H. Haugan[73], J. Hoar[33], H. Hoekstra[74], W. Holmes[75], I. Hook[76], F. Hormuth[77], A. Hornstrup[78,79], P. Hudelot[80], K. Jahnke[11], E. Keihänen[81], S. Kermiche[69], A. Kiessling[75], T. Kitching[49], R. Kohley[33], B. Kubik[58], M. Kümmel[38], M. Kunz[82], H. Kurki-Suonio[83,84], O. Lahav[85], S. Ligori[39], P. B. Lilje[73], V. Lindholm[83,84], I. Lloro[86], E. Maiorano[7], O. Mansutti[68], O. Marggraf[87], K. Markovic[75], N. Martinet[13], F. Marulli[88,7,36], R. Massey[89], S. Maurogordato[32], H. J. McCracken[80], E. Medinaceli[7], S. Mei[90], M. Melchior[91], Y. Mellier[29,80], M. Meneghetti[7,36], E. Merlin[27], G. Meylan[24], M. Moresco[88,7], L. Moscardini[88,7,36], E. Munari[68,92], R. C. Nichol[93], S.-M. Niemi[9], J. W. Nightingale[94,95], C. Padilla[96], S. Paltani[62], F. Pasian[68], K. Pedersen[97], W. J. Percival[22,23,98], V. Pettorino[9], S. Pires[6], G. Polenta[99], M. Poncet[100], L. A. Popa[101], L. Pozzetti[7], G. D. Racca[9], F. Raison[1], R. Rebolo[3,4], A. Renzi[102,64], J. Rhodes[75], G. Riccio[43], H.-W. Rix[11], E. Romelli[68], M. Roncarelli[7], E. Rossetti[35], R. Saglia[38,1], D. Sapone[103], B. Sartoris[38,68], M. Sauvage[6], R. Scaramella[27,104], P. Schneider[87], T. Schrabback[19], A. Secroun[69], G. Seidel[11], M. Seiffert[75], S. Serrano[66,105,106], C. Sirignano[102,64], G. Sirri[36], J. Skottfelt[107], L. Stanco[64], P. Tallada-Crespí[51,52], A. N. Taylor[55], H. I. Teplitz[108], I. Tereno[60,26], R. Toledo-Moreo[109], F. Torradeflot[52,51], I. Tutusaus[110], E. A. Valentijn[10], L. Valenziano[7,111], T. Vassallo[38,68], G. Verdoes Kleijn[10], A. Veropalumbo[34,41,112], Y. Wang[108], J. Weller[38,1], O. R. Williams[113], G. Zamorani[7], E. Zucca[7], A. Biviano[68,92], C. Burigana[114,111], G. De Lucia[68], K. George[38], V. Scottez[29,115], P. Simon[87], A. Mora[116], J. Martín-Fleitas[116], F. Ruppin[58], and D. Scott[117]

*(Affiliations can be found after the references)*

May 22, 2024

**ABSTRACT**

We study the intracluster light (ICL) and intracluster globular clusters (ICGCs) in the nearby Perseus cluster of galaxies using *Euclid*'s Early Release Observations. By modelling the isophotal and iso-density contours, we map the distributions and properties of the ICL and ICGCs out to a radius of 600 kpc ($\sim \frac{1}{3}$ of the virial radius) from the brightest cluster galaxy (BCG). We find that the central 500 kpc of the Perseus cluster hosts 70 000 ± 2800 globular clusters, and $1.6 \times 10^{12}$ $L_\odot$ of diffuse light from the BCG+ICL in the near-infrared $H_E$. This accounts for 37 ± 6% of the cluster's total stellar luminosity within this radius. The ICL and ICGCs share a coherent spatial distribution which suggests that they have a common origin or that a common potential governs their distribution. Their contours on the largest scales (> 200 kpc) are not centred on the BCG's core, but are instead offset westwards by 60 kpc towards several luminous cluster galaxies. This offset is opposite to the displacement observed in the gaseous intracluster medium. The radial surface brightness profile of the BCG+ICL is best described by a double Sérsic model, with 68 ± 4% of the $H_E$ light contained in the extended, outer component. The transition between these components occurs at ≈50 kpc, beyond which the isophotes become increasingly elliptical and off-centered. Furthermore, the radial ICGC number density profile closely follows the profile of the BCG+ICL only beyond this 50 kpc radius, where we find an average of 60 globular clusters per $10^9$ $M_\odot$ of diffuse stellar mass. The BCG+ICL colour becomes increasingly blue with radius, consistent with the stellar populations in the ICL having subsolar metallicities [Fe/H] ∼ −0.6. The colour of the ICL, and the specific frequency and luminosity function of the ICGCs suggest that the ICL+ICGCs were tidally stripped from the outskirts of massive satellites with masses of a few $\times 10^{10}$ $M_\odot$, with an increasing contribution from dwarf galaxies at large radii.

**Key words.** Galaxies: clusters: individual: Abell 426, Galaxies: clusters: intracluster medium, Galaxies: individual: NGC 1275, Globular clusters: general

## 1. Introduction

Over the last 20 years, observations have shown that the intracluster light (ICL) is a ubiquitous feature in galaxy clusters (e.g., Feldmeier et al. 2004; Kluge et al. 2020; Golden-Marx et al. 2023). As the byproduct of interactions between galaxies in clusters (e.g., Gregg & West 1998; Mihos et al. 2005), the ICL is a fossil record of all the dynamical interactions the system has experienced and offers a holistic view of the cluster's history (see Contini 2021 and Montes 2022 for reviews). Thus, the origin and assembly history of the ICL is central to understanding the global evolution of the cluster galaxy population.

In addition, the ICL has been shown to be a tool for inferring the radius of the cluster and even its dark matter distribution (Montes & Trujillo 2019; Alonso Asensio et al. 2020; Deason et al. 2021; Gonzalez et al. 2021; Yoo et al. 2022; Contreras-Santos et al. 2024). Despite being such a useful tool for understanding our Universe, our knowledge of this component is limited because the ICL is faint ($\mu_V > 26.5$ mag arcsec$^{-2}$, Rudick et al. 2006) and extended (hundreds of kpc), so we need deep and wide-field observations to study it.

The accretion events that form this diffuse light also bring large numbers of globular clusters (GCs) into the intracluster space, which we refer to as intracluster globular clusters (ICGCs) (e.g., Durrell et al. 2014; Alamo-Martínez & Blakeslee 2017; Lee et al. 2022). These luminous tracers are an additional clue to infer the past history of the cluster. Moreover, Reina-Campos et al. (2023) show that the GCs can also be used to trace the dark matter distribution in halos.

The *Euclid* (Laureijs et al. 2011; Euclid Collaboration: Mellier et al. 2024) space mission will observe nearly one-third of the sky in four photometric bands: one in the visible ($I_E$) using the VIS instrument (Euclid Collaboration: Cropper et al. 2024) and three in the near-infrared (NIR; $Y_E$, $J_E$, $H_E$) using the NISP instrument (Euclid Collaboration: Jahnke et al. 2024). The faint detection limit, the design of the wide-field telescope, and the tight control on the scattered light makes *Euclid* ideal to study the low surface-brightness (LSB) Universe (Euclid Collaboration: Scaramella et al. 2022; Euclid Collaboration: Borlaff et al. 2022), in particular the ICL.

In this work, we analyse the ICL and ICGCs of the Perseus cluster of galaxies (Abell 426). The images analysed here are part of the Early Release Observations (ERO) programme, a collection of observations dedicated to showcasing *Euclid*'s capabilities. Perseus is located close to the Galactic plane and therefore is awash with Galactic cirri, and suffers from high and spatially varying extinction. It is therefore a highly complex case study that we use to demonstrate the potential of *Euclid* for LSB research, even in difficult conditions.

The Perseus galaxy cluster is one of the most spectacular nearby astronomical objects. It is a low-redshift ($z = 0.0179$), massive, rich Bautz-Morgan class II-III galaxy cluster with a velocity dispersion of $1040^{+34}_{-43}$ km s$^{-1}$ (Aguerri et al. 2020) and is the brightest X-ray cluster in the sky in terms of flux (Edge et al. 1992). X-ray observations report that the virial radius of this cluster ($r_{200,c}$) is 1.79 Mpc (82′ on the sky, Simionescu et al. 2011), which encloses a total mass ($M_{200,c}$) of $(6.65 \pm 0.5) \times 10^{14}$ M$_\odot$, making it one of the most massive nearby clusters. The mass and virial radius derived through optical spectroscopy are a factor of 1.8 and 1.2 larger than this, respectively (Aguerri et al. 2020). Although this cluster has been studied in many previous observations, *Euclid*'s field-of-view (0.57 deg$^2$), superb spatial resolution and low background means these observations are the first in-depth, high-resolution look at the Perseus cluster as a whole from the optical to the near-infrared, allowing for a detailed study of the intracluster stellar population.

For simplicity, in this work we refer to the diffuse light beyond 100 kpc of the brightest cluster galaxy (BCG) as ICL. At the same time, the GCs beyond this radius are identified as ICGCs. This definition is supported by observations that find a break radius in the BCG+ICL light profile at 60–80 kpc (Zibetti et al. 2005; Gonzalez et al. 2005; Iodice et al. 2016; Zhang et al. 2019; Montes et al. 2021), and the stellar tracers across this boundary display different kinematics (e.g., Longobardi et al. 2018; Hartke et al. 2023). By defining the ICL and ICGCs as existing beyond this radius, we make sure that the influence of the light and GCs from the BCG is minimal.

The luminosity distance of the Perseus cluster is $(72 \pm 3)$ Mpc, or alternatively, $m - M = 34.3 \pm 0.1$ mag (Tully et al. 2023), which corresponds to an angular diameter distance of 0.338 kpc arcsec$^{-1}$. We assume a standard flat $\Lambda$CDM cosmology with $\Omega_m = 0.319$ and $H_0 = 67$ km s$^{-1}$Mpc$^{-1}$ (Planck Collaboration: Aghanim et al. 2020), and all magnitudes are given using the AB magnitude system.

## 2. Observations

We use the ERO images (Euclid Early Release Observations 2024) of the Perseus cluster taken by ESA's *Euclid* satellite (Euclid Collaboration: Mellier et al. 2024). The observations are centred on the position RA = 3$^h$ 18$^m$ 40, Dec = 41° 39′ 00, have a field-of-view of $\sim 0.7$ deg$^2$, and are rotated clockwise by 30° relative to north. The images were obtained in a dithered observation sequence that is similar to the Reference Observation Sequence (ROS) that will be used to observe the *Euclid* Wide Survey (EWS; Euclid Collaboration: Scaramella et al. 2022). In this sequence, an image in $I_E$ is taken simultaneously with slitless grism spectra in the NIR, followed by NIR images taken in $J_E$ then $H_E$, and finally $Y_E$. The telescope is then dithered and the sequence is repeated three further times. Four ROS were combined to make the final Perseus images, whereas the EWS will only be at the depth of one ROS.

The resulting images of the Perseus cluster have a maximum exposure time of 9056 s in $I_E$, 1395.2 s in $Y_E$, $J_E$, and $H_E$. The $I_E$ images have a pixel scale of 0.1 arcsec pix$^{-1}$, and a spatial resolution (FWHM) of 0.″16. The NIR images have a pixel scale of 0.3 arcsec pix$^{-1}$, and a spatial resolution of $\sim$ 0.″49. Further details on these images are provided in Cuillandre et al. (2024b). The images were processed according to the method described in the accompanying article (Cuillandre et al. 2024a), which has been optimised to preserve the LSB emission in each image. Figure 1 shows a $Y_E$, $J_E$, $H_E$ false-colour image centred on the two brightest galaxies in the Perseus cluster: the BCG, NGC 1275, and its companion NGC 1272. It illustrates that the ICL signal is preserved out to many arcminutes.

⋆ This paper is published on behalf of the Euclid Consortium.
⋆⋆ e-mail: nina.hatch@nottingham.ac.uk

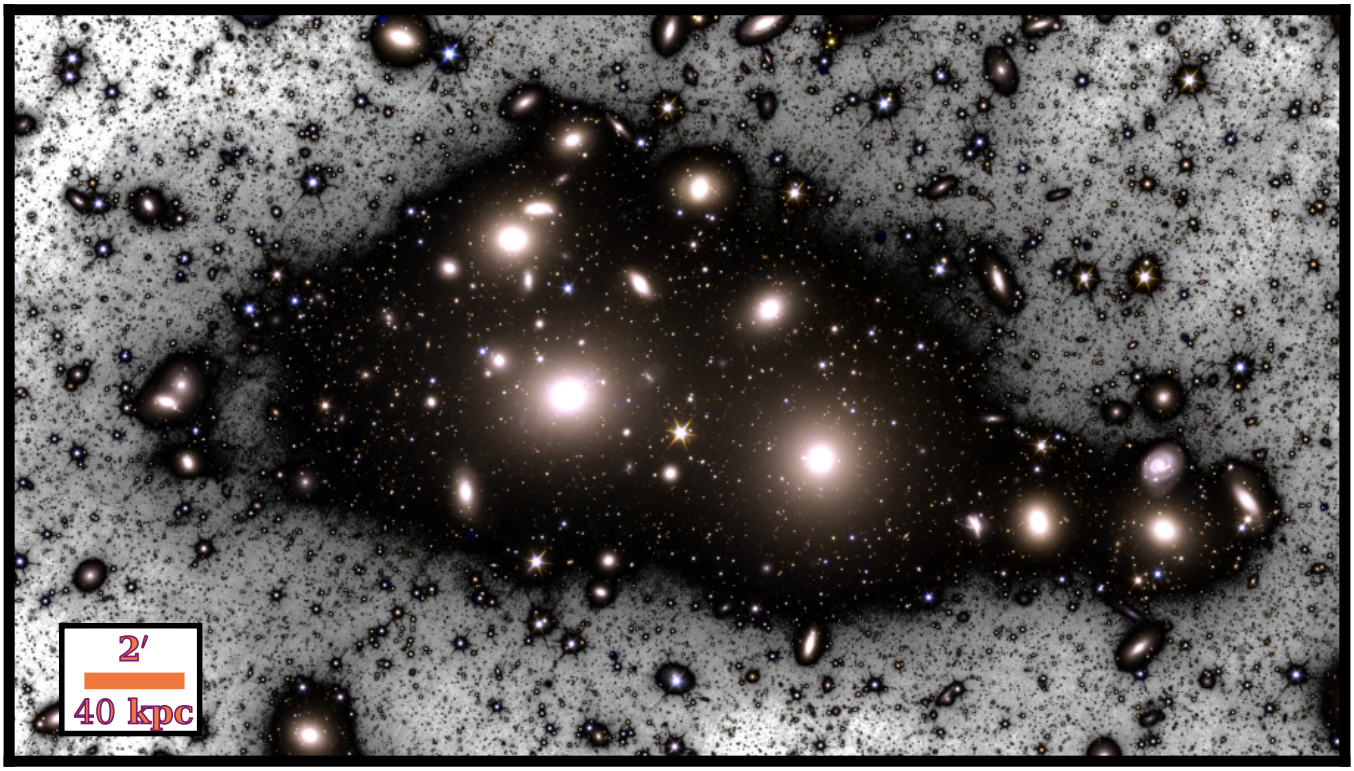


**Fig. 1.** A region of 26′×15′ around the centre of the Perseus cluster of galaxies. The figure is a composite of an RGB image using the $I_E$, $J_E$, and $H_E$ bands, respectively, and a combined $I_E + J_E + H_E$ image used for the inverted black and white background. North is up, east is left. The brightest two galaxies in this image are the BCG, NGC 1275, to the left, and NGC 1272 to the right.

## 3. Data processing

The ERO were detrended following the steps outlined in Cuillandre et al. (2024a), including: overscan correction and bias structure correction, flat fielding on median and large scales using the zodiacal light as a flat illumination source to produce images that appear background-flat, flat fielding on small scales using calibration flats, and detector to detector image scaling. These processes ensure the continuity of the extended emission but limit the accuracy of the photometry to a few percent.

The LSB emission in the NISP images is strongly impacted by persistence (see figure 11 in Cuillandre et al. 2024a), and accurate measurements of the ICL cannot be made without removing this strong signal. Since masking the persistence would lead to large holes in the stacked images, the persistence was modelled and subtracted in the individual exposures before the exposures were stacked. Details of this modelling are provided in Cuillandre et al. (2024a). Following these processing steps, the $1\sigma$ depths of the LSB-optimised images are $\mu(I_E) = 30.5\,\mathrm{mag\,arcsec^{-2}}$ and $\mu(Y_E, J_E, H_E) = 28.7, 28.9, 28.9\,\mathrm{mag\,arcsec^{-2}}$, measured over a $10'' \times 10''$ area, and expressed as asinh AB magnitudes.

The Perseus ERO was affected by low-level scattered light in VIS on the level of 3%–4% of the zodiacal light (Euclid Collaboration: Mellier et al. 2024) which will impact the ICL measurements in $I_E$. Therefore, in addition to the data processing described in Cuillandre et al. (2024a), we applied the following processing steps that are essential for accurate diffuse LSB photometry:

- The modelling and removal of a large-scale gradient in the $I_E$ image.
- The modelling and removal of Galactic cirri from the $I_E$ image.
- The modelling and subtraction of the large-scale point spread function (PSF) for the brightest stars in the field-of-view, which was applied to the $I_E$ and NIR images.

These steps are visualised in Fig. 2.

The initial $I_E$ image had a large-scale east-west gradient with background inhomogeneities of the order of $26\,\mathrm{mag\,arcsec^{-2}}$ (see Fig. 2a), which corresponds to 3% – 4% of the background flux. Stray light on that level had been noticed in the VIS detector (Euclid Collaboration: Mellier et al. 2024). This strong gradient is neither apparent in the NIR images nor in a deep $i'$-band image of the Perseus cluster (see Fig. 2e), that was observed with the Canada-France-Hawaii Telescope[1] (CFHT). Regardless of its origin (whether astronomical or stray light in the telescope), this light gradient is a contaminant to the ICL, so we removed it.

Unfortunately, the gradient is more complex than can be described by a 2-D first-order polynomial because it falls off steeper in the west. Fitting higher-order functions to the background can result in overfitting and removing part of the ICL. To avoid this, we matched the $I_E$ background to that of the CFHT image. This image is well suited for this task because its back-

[1] Details of the CFHT images of Perseus, and how they were optimised for LSB emission, can be found in Cuillandre et al. (2024b). The $I_E$ image has advantages over the CFHT $i'$-band image for detecting GCs (see Fig. 3) and the ICL due to its compact PSF and minimal PSF wings, significantly reducing PSF broadening effects on the surface brightness and colour profiles (Duc et al. 2015; Trujillo & Fliri 2016; Kluge et al. 2020) and allowing us to explore the ICL in the critical region between NGC 1275 and NGC 1272 near a bright contaminating star (see Fig. 1).

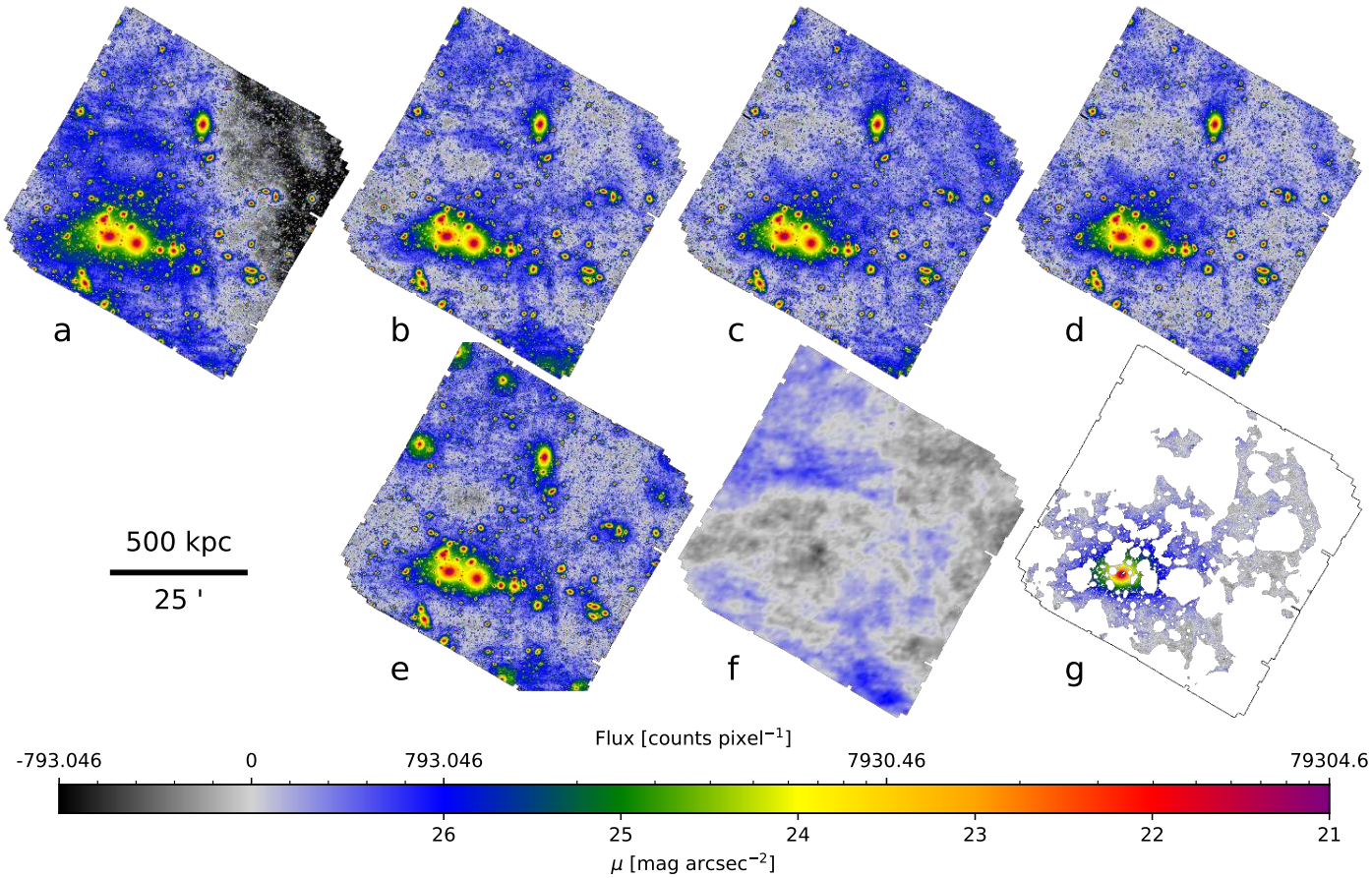


**Fig. 2.** All panels show the full field-of-view of the $I_E$ image. The panels show: (a) the original $I_E$ image with an east-west gradient visible in the background, (b) the $I_E$ image that has been flattened to match the background properties of the CFHT $i'$-band image (which is shown in panel e), (c) is the image after the subtraction of a scaled 12µm WISE image (shown in panel f) to remove Galactic cirri and the PSF subtraction has been performed on 75 of the brightest stars in the field-of-view. Panel (d) shows the final processed $I_E$ image after a 2D first-order polynomial gradient was subtracted from the background. Panel (g) shows only the area of the image that is left unmasked, after the light profile of NGC 1272 has been subtracted. The scaling of the colour map transitions smoothly from logarithmic to linear steps at low fluxes in order to highlight the patterns in the background.

ground is much flatter and it is sufficiently deep: the same structures in the ICL and the cirri are visible in both Figs. 2a and 2e (e.g., diffuse emission with $\mu(I_E)$ ~26 mag arcsec$^{-2}$ in the north, west, and south image corners) and they are fainter than the artificial gradient observed in Fig. 2a.

First, the CFHT image was subtracted from the *Euclid* $I_E$ image. Subsequently, a 2D fourth-order polynomial was fit to the residuals. This polynomial was then subtracted from the original $I_E$ image, producing the final image shown in Fig. 2b.[2] This step will not be required in future *Euclid* data releases since the low-level scattered light in VIS will be modelled and removed in the pipeline processing of the data.

Galactic cirri are prominent at optical wavelengths but less so at NIR wavelengths (e.g., Román et al. 2020). Therefore we modelled and removed Galactic cirri from the $I_E$ image, but not the NIR images. To do so, we extracted the region of the Perseus ERO from the dust emission maps by Meisner & Finkbeiner (2014, Fig. 2f). This map was generated from the WISE 12 µm imaging data and is free of compact sources and other contaminating artifacts. The angular resolution is limited by the highest HEALPIX resolution of NSIDE = 8192, corresponding to ~26″ per pixel.

We normalised this map to match the average background properties of the $I_E$ image (Fig. 2b). We find that the brightest patches of Galactic cirri in this region have a surface brightness of $\mu(I_E)$ = 26 mag arcsec$^{-2}$. To create the image shown in Fig. 2c, we then subtracted this low-resolution cirri image from the $I_E$ image.

Unfortunately, the resulting image (Fig. 2c) displays a slight flux gradient that is likely an artifact produced from incorrect cirri subtraction and the need to perform the CFHT-image flattening before the cirri subtraction. We therefore fitted a 2D first-order polynomial gradient[3] to the masked image and subtracted it from the final $I_E$ image. This gradient is opposite to the first gradient but the amplitude is four times smaller. We used the resulting image, shown in Fig. 2d, for the remaining analysis.

At the time of analysis, large-scale PSF models were not available, so we constructed empirical PSFs for each image ($I_E$, $Y_E$, $J_E$, and $H_E$). We first created postage stamps of ~100 bright

[2] The amplitude of the linear gradient is comparable to the perturbations described by the higher orders. We cannot conclude whether the high-order terms are significant because instrument-based inhomogeneities in the CFHT background cannot be excluded. Different PSF shapes have no impact on the matched background pattern. They lead to strong small-scale outliers that are discarded by sigma clipping. Furthermore, prominent PSF ghosts from the CFHT image were masked in the residual image.

[3] We did not fit a higher-order function as it can lead to oversubtraction of the ICL.

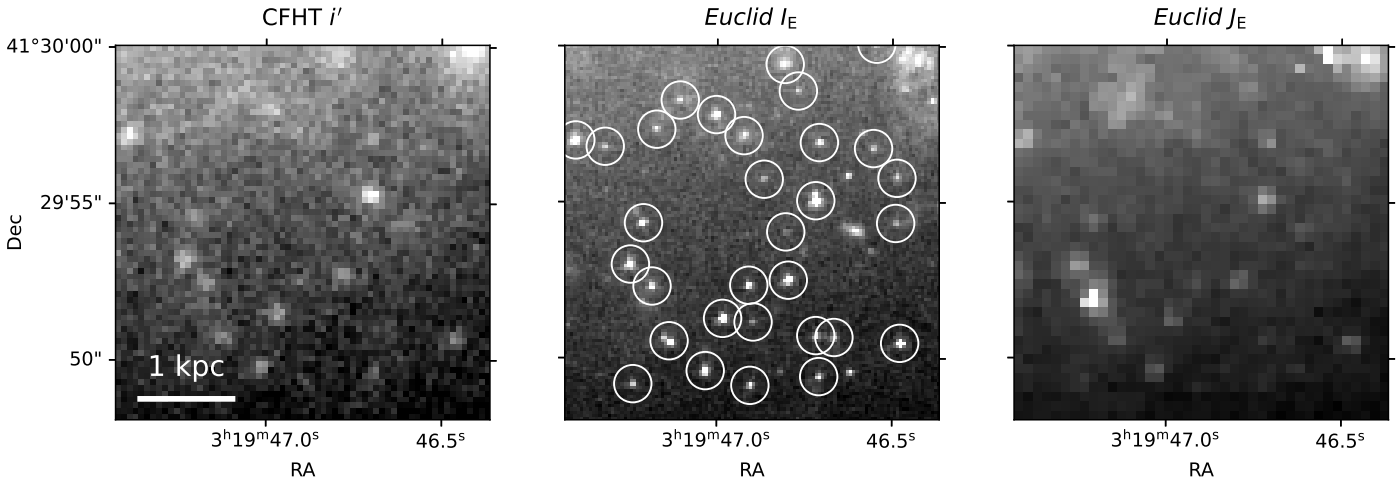


**Fig. 3.** A zoomed-in of the Perseus ERO focusing on a region that lies 17 kpc southwest of NGC 1275. The ground-based seeing-limited CFHT $i'$-band image (left panel) is comparable in wavelength to the *Euclid* $I_E$-band image (middle panel). However, the superior spatial resolution in $I_E$ reveals numerous GCs, which are encircled in white. *Euclid*'s resolution decreases with wavelength because of diffraction and undersampling of the PSF, such that most of the GCs cannot be identified in the $J_E$ band (right panel). Black and white correspond to a surface brightness of $\mu$ = 22 and 21 mag arcsec$^{-2}$, respectively, in the left and middle panels, and $\mu(J_E)$ = 23 and 22 mag arcsec$^{-2}$ in the right panel.

stars with magnitudes in the range $11.5 < I_E < 13.6$. Our goal was not to accurately subtract the PSF core, which is saturated for these bright stars, but rather to accurately subtract the outer PSF profile where the star's diffuse light can be confused with ICL (e.g., Montes et al. 2021). For $I_E$ we used postage stamps of 1400 pixels (140″) on a side, while for the NIR bands, the postage stamps were 500 pixels (150″) on a side. We masked bright sources in each postage stamp (excluding the diffraction spikes), then median combined the stamps to obtain a PSF.

The PSF model was then subtracted from the 75 brightest stars in the Perseus field, excluding those stars located near the edge of the field or those located close to another bright source (which prevented the outer profile of the star from being accurately measured). The same stars were subtracted in each of the $I_E$, $Y_E$, $J_E$, and $H_E$ images. We note that some of these stars were used in the construction of the PSF. To ensure the best subtraction of the outer profile, we normalised the PSF profiles using a carefully selected aperture around each star that minimizes the chi-squared statistic for the difference between the normalized PSF and the outer light profile of the individual star.

## 4. Detecting the intracluster stellar tracers

We use two tracers of intracluster stars in this analysis: the ICL and ICGCs. The ICL presents as diffuse LSB emission, while GCs at the distance of the Perseus cluster appear as faint point sources embedded in the ICL and throughout the halos of bright cluster galaxies. The method to measure these two sources diverges at this point in the analysis, and we describe both methods in turn.

### 4.1. Isolating the intracluster light

Precise surface photometry of the ICL requires complete and homogeneous masks where only the BCG and ICL remain unmasked, so we aggressively masked the remaining high surface-brightness regions of the images, including all GC candidates. We applied the method described in Kluge et al. (2020) and Kluge (2020). In brief:

- Images were "flattened" by subtracting a spline-based background to remove the diffuse light or other LSB features. The spline step size varies between 50 and 100 pixels (independent of the pixel scale) for different masks depending on the source sizes. This step is necessary to avoid masking the BCG+ICL.
- Flattened images were then smoothed to optimally identify objects on various spatial scales while avoiding the masking of noise peaks misidentified as signals. The standard deviation of the Gaussian smoothing kernel varies between 3 and 15 pixels for different masks, while larger spatial scales were handled by median-binning by 20 pixels × 20 pixels and re-applying the masking procedure.
- Masks were derived on the smoothed and flattened images by applying signal-to-noise scaled surface brightness thresholds that are optimized for each spatial scale.
- A manual re-masking was applied to the star-forming regions of NGC 1275 (Conselice et al. 2001; see Fig B.2) as well as the outskirts of very extended sources and background inhomogeneities on arcminute scales (due to, e.g., Galactic cirri residuals or isolated patches of ICL detached from the BCG).
- This procedure was repeated in the inner regions of NGC 1275 and NGC 1272 after the galaxies' models have been subtracted from the images (see Sect. 4.3) to ensure that the stellar halos of galaxies near these bright galaxies are also masked.
- Masks were generated for each of the four images separately, and the union of these masks was used to create a single mask that was applied to all images for the ICL analysis.

The resulting limiting surface brightness for 2-D structures can be estimated by inspecting Fig. 2g. The large-scale variations in the remaining unmasked regions are of the order of 27 mag arcsec$^{-2}$.

### 4.2. Detecting intracluster globular clusters

Most GCs are embedded in the BCG and the surrounding ICL, so we constructed a new source catalogue that includes sources embedded within the high surface-brightness regions. We first removed as much of the diffuse light as possible by applying a

ring median filter, with $R_{\rm in}$ = 2 pixels and $R_{\rm out}$ = 4 pixels, to derive a filtered image of the $I_{\rm E}$ image. This filtered image was subtracted from the $I_{\rm E}$ image, and the resulting residual image was used for source detection.

Objects were detected using the `astropy.photutils` python package (Bradley et al. 2023) by selecting sources with 3 connected pixels with a flux threshold of at least 3 times the root-mean-square (RMS) statistic of the background. To ensure even detection across the entire field-of-view we masked regions that were observed for less than 30% of the total exposure time.

Photometry and shape measurements of the sources were made on the original image (Fig. 2d). Background-subtracted photometry was measured in circular apertures with radii of 2 and 5 pixels, with a median background measured in an annulus with $R_{\rm in}$ = 7 pixels and $R_{\rm out}$ = 13 pixels. We corrected for Galactic extinction using the *Planck* thermal dustmap (Planck Collaboration: Abergel et al. 2014), Gordon et al. (2023) extinction law, and assuming an SED of a 5700 K blackbody.

GC candidates were selected as sources with an aperture-corrected magnitude in the range $22.7 < I_{\rm E} < 26.3$, an FWHM less than 4 pixels, elongation less than 2, and a concentration index (the difference between the uncorrected aperture magnitude measured at 2 and 5 pixels, Peng et al. 2011) between 0 and 1 mag. The faint magnitude limit corresponds to the approximate turn-over magnitude for GCs at the distance of the Perseus cluster. The bright limit is equivalent to $3\sigma$ brighter than the turn-over magnitude assuming the GC luminosity function (GCLF) has an approximately Gaussian spread of $\sigma \sim 1.2$ mag. Figure 3 shows an exemplary image highlighting the numerous GC candidates that are visible in the high spatial resolution $I_{\rm E}$ band (middle panel), whereas most cannot be detected in the $J_{\rm E}$ band (right panel) and the seeing-limited CFHT image (left panel).

We note that the above criteria also select Milky Way stars and small background galaxies. We removed some of these contaminating sources using an `astropy.photutils` segmentation map of sources that are larger than 4 arcsec$^2$, and that are twice the RMS of the background. We removed any GC candidate that overlaps with these extended sources. This segmentation map also masks the brightest features of the emission-line nebula of NGC 1275, and the high-velocity system of NGC 1275 that overlaps the northwestern part of the BCG. There are several bright star clusters embedded in these systems (Canning et al. 2010), but the GCs would only be co-spatial with the line-emitting filaments for a relatively short time ($10^8$ yr), so we are not likely missing a large fraction of the GCs in this system.

This work focuses on the GCs in the BCG and the intracluster region so we removed GCs associated with the other cluster galaxies. Using the $I_{\rm E}$ image as the detection image (Fig. 2d), we created a background RMS map by obtaining a median filtered map on the scale of a square box of 1000 pixels on a side. Large objects were selected as sources that have 50 000 connected pixels that are 3.5 times the RMS of the background. Candidate GCs within the large objects were removed from the GC candidate catalogue, except for candidate GCs within the BCG and the nearby bright galaxy NGC 1272. The GCs within NGC 1272 were modelled and removed statistically (see Sect. 4.3), rather than masked, as the galaxy is very close to the cluster core.

The remaining candidate GCs will still include contamination from faint stars and point-like background galaxies, which are assumed to have a uniform distribution over the field. These contaminants were removed via statistical background subtraction in the results shown below. The number density of these contaminants is described in Appendix A.

### 4.3. Modelling of ICL surface brightness profiles and ICGC density profile

Our approach to modelling the ICL is based on fitting ellipses to lines of constant surface flux (isophotes). The biggest advantage of this approach over 2-D parametric image modelling is that we obtain radial profiles of the surface brightness, ellipticity, position angle, and centring. However, a disadvantage arises when galaxies overlap because the isophotes cannot be approximated by ellipses; iterative modelling is necessary in such cases. In addition to the BCG, the Perseus cluster core contains another bright galaxy, NGC 1272, that is only 1 magnitude fainter (in $I_{\rm E}$) and lies only 5′ (105 kpc) from NGC 1275. The close proximity of a bright cluster galaxy complicates the modelling of the BCG+ICL light profile and BCG+ICGC density profile. We therefore modelled and subtracted the second-ranked cluster galaxy (in both diffuse light and GC surface density) before measuring the BCG+ICL light profile and the BCG+ICGC density profile.

We began by modelling NGC 1275 and subtracting this model from the image. We then modelled NGC 1272 and subtracted it from the original image before remodelling NGC 1275. To minimize the contamination due to overlapping isophotes, the surface brightness profile of NGC 1272 was extrapolated beyond a semi-major axis radius of $a \approx 200''$ using the best-fit Sérsic profile ($n \approx 1.0$).

We fitted ellipses to the isophotes using the `ellipse` task from the python package `photutils` (Bradley et al. 2023). Each ellipse has four free parameters: the central coordinates, $x_0$ and $y_0$, the ellipticity, $\epsilon = 1 - b/a$ (where $a$ is the semi-major axis radius and $b$ is the semi-minor axis radius), and the position angle, PA (counting anticlockwise starting from the horizontal line). The semi-major axis radius, $a$, was chosen to increase in logarithmic steps by 10% for each isophote. As the ICL becomes fainter at larger radii, some ellipse parameters could not be measured robustly. This happened when the parameters changed significantly and randomly for sequential isophotes. At this point, we fixed the parameters to the last robust isophote for which their values were successfully measured.

The flux along the isophotes where $a < 15$ pixels was measured using `ellipse`. However, for $a > 15$ pixels, we took the median value of all unmasked pixels in an elliptical annulus around that isophote, which produces equivalent results but is computationally more efficient. The width of the annulus is equivalent to the step size at the radius, which is selected to extract the maximum signal-to-noise while avoiding overlaps between different annuli. We generated model BCG+ICL images by interpolating the 1-D isophotal shape profiles onto a fine grid with 1000 steps equidistant in $a^{1/4}$. The corresponding annuli were filled with the surface flux at the given radius.

A similar method was used to determine a simplified model of the BCG+ICGC distribution by fitting ellipses to lines of constant GC surface density (iso-density contours). GCs are spatially distinct point sources but computing the shape of their global distribution requires a smooth map. Therefore, we computed the surface density of GC candidates in bins of 40″ on a side. We then used this map of GC surface density to fit iso-density contours to the GC distribution using the same method as described above.

To increase the maximum radius to which the GC iso-density contours can be fitted robustly, we smoothed the image using a Gaussian kernel with $\sigma = 56''$ and repeated the procedure. Both profiles, one representative of the inner region and one of the outer region of the ICGC distribution, were merged at $a = 450''$.

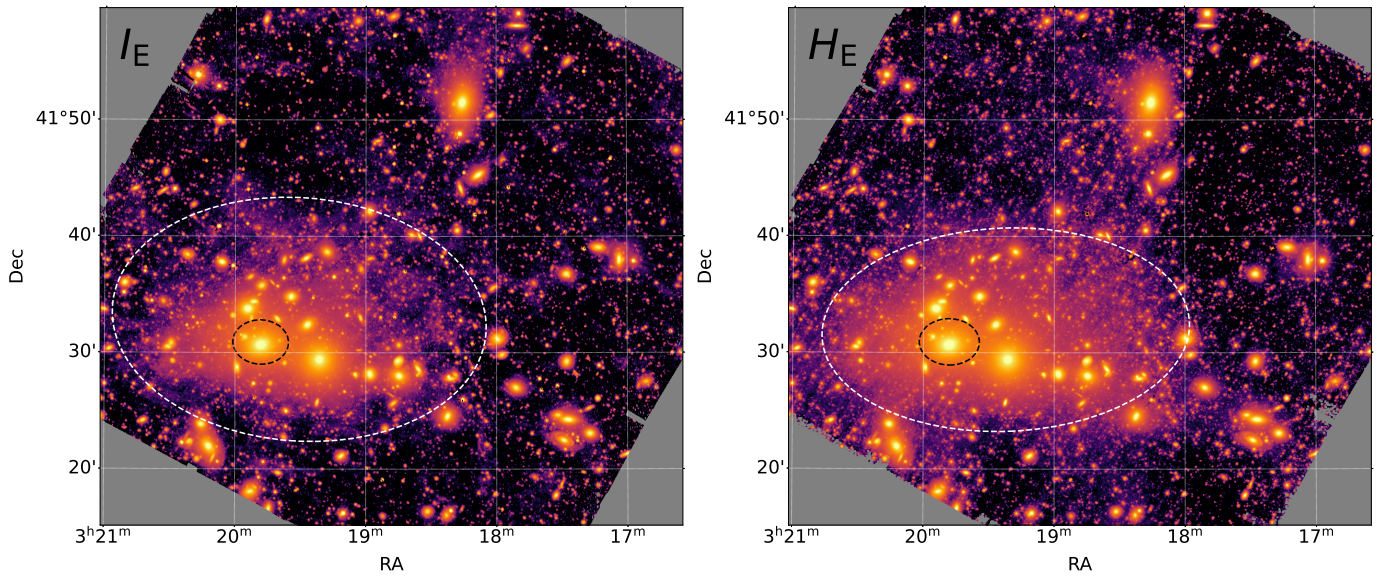


**Fig. 4.** The processed $I_E$ image (left) and $H_E$ image (right). The log-normal colour scheme is used to emphasize the ICL. We masked small, bright sources and interpolated over the maskedm pixels using a Gaussian kernel with a standard deviation of $\sigma = 30$ and 6 pixels for the $I_E$ and $H_E$ images, respectively. To guide the eye, we show the isophotal contours with a semi-major axis of $a = 50$ kpc (black) and 320 kpc (white).

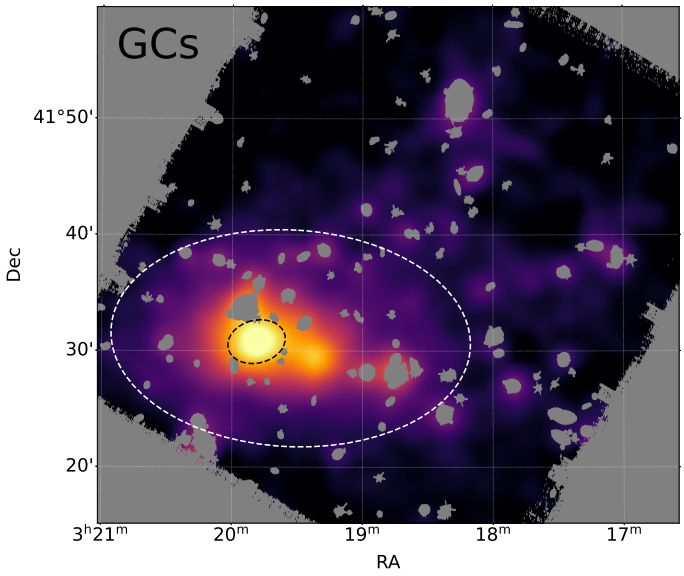


**Fig. 5.** This map of the number density distribution of GC candidates was produced by modelling each GC candidate as a single pixel with unity flux, which was then smoothed with a Gaussian kernel of $\sigma = 50''$. The colour scheme therefore represents the GC number density. We masked bright stars, diffraction spike residuals, the emission line nebula, and the high-velocity system of NGC 1275, as well as large cluster galaxies (except for the NGC 1275 and its nearby companion in the west, NGC 1272). Iso-density contours with a semi-major axis of $a = 50$ kpc (black) and 320 kpc (white) are shown for the GC candidates.

We checked that the smoothed profiles converge sufficiently to the unsmoothed profiles at $a = 450''$.

Once the position of the iso-density contours was defined, we calculated the mean density of GCs in an elliptical annulus around the contours using the unsmoothed and unbinned GC candidate catalogues, and taking into account the masked area of each annulus. The width of each annulus is equivalent to the step size at that radius. To construct the profile around NGC 1275, we masked both NGC 1272 and NGC 1265 (the brightest galaxy in the north of the field-of-view) with ellipses with $a = 100$ kpc to minimise the contamination of GCs from the halos of these galaxies.

Ideally, the background constant of the BCG+ICL surface brightness and GC surface density would be measured beyond the virial radius of the cluster, well beyond the region where ICL may exist. However, due to the large extent of the Perseus ICL on the sky, which goes beyond the observed field-of-view, we determined the residual background flux/GC surface density by hand as the value to which the surface flux/density profile converges at large radii. Further details on the background measurement and uncertainties are provided in Appendix A. The full images, masks, residuals, and models for the BCG+ICL in all four filter bands, and the GC surface density measured in $I_E$, are shown in Appendix B.

## 5. Results

### 5.1. Distribution of the BCG+ICL and GCs

Figure 4 presents the $I_E$ and $H_E$ images with a colour bar chosen to accentuate the ICL. To further highlight the ICL – rather than be distracted by small, high surface-brightness sources – we masked small, bright sources and interpolated over these pixels using a Gaussian kernel of $\sigma = 30$ pixels and 6 pixels for the $I_E$ and $H_E$ images, respectively.

The GC number density map, shown in Fig. 5, was produced by modelling each GC candidate as a single $I_E$ pixel with unity flux. We then smoothed this map with a Gaussian kernel with $\sigma = 50''$ and took care to properly interpolate over the masked regions of the image. The colour scheme therefore represents the GC number density. NGC 1272 was not masked in this image because we fitted a model to its GC distribution and subtracted it before measuring the iso-density contours. The GCs of NGC 1272 are distributed in a compact circular configuration, extending no more than 100 kpc from the galaxy's core.

Two of the fitted contours are shown on Figs. 4 and 5 to illustrate the best-fit ellipses on both small and large scales. The

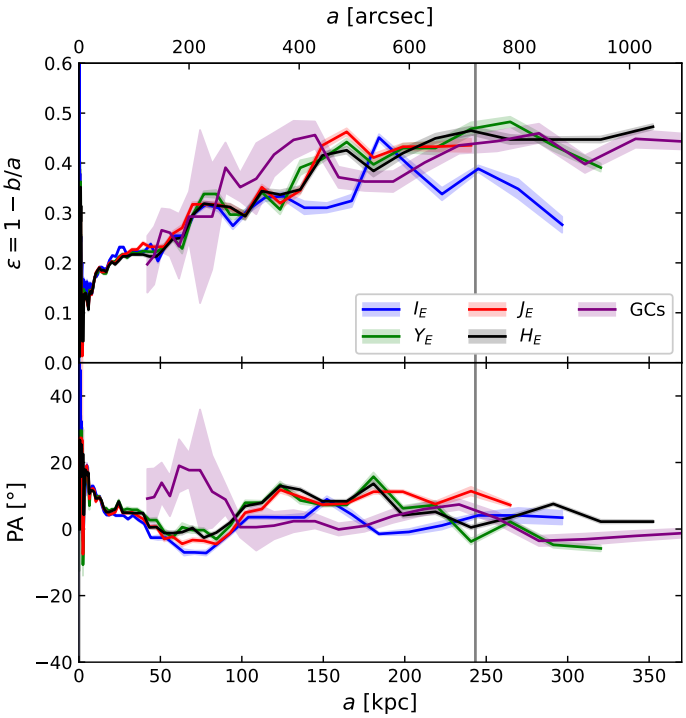


**Fig. 6.** The ellipticities and position angles (PA) of the ellipses fit to isophotes of the BCG+ICL in the $I_E$, $J_E$, $Y_E$, and $H_E$ images and iso-density contours of the GC map. The GC distribution was binned to a pixel scale of 40″, therefore only data beyond 120″ radius are shown. The vertical line indicates the radius $a = 12'$ beyond which background inhomogeneities could alter the profiles of the ICL (see Appendix A).

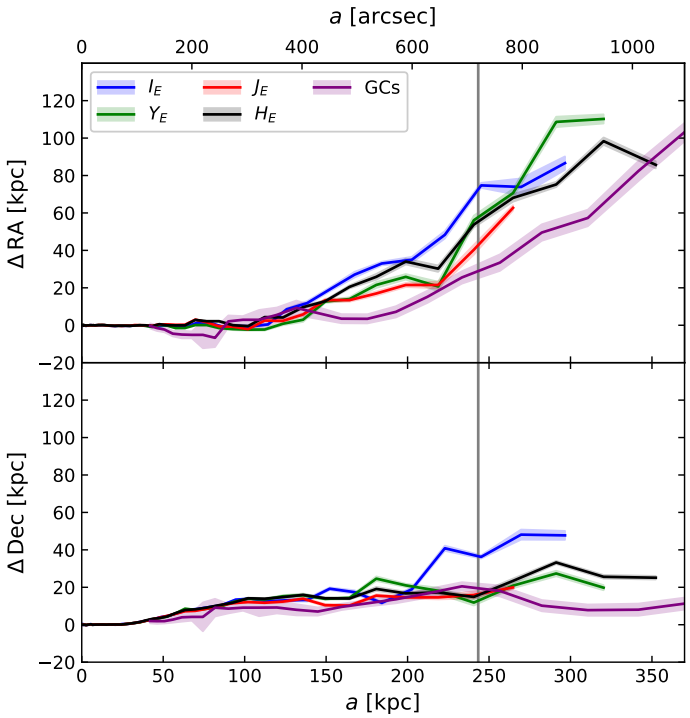


**Fig. 7.** The offset of the RA (top) and Dec (bottom) centroid of the isophotal/isodensity elliptical contours in all four images and the intracluster GCs map. The Δ RA = 0 and Δ Dec = 0 points are defined as the position of the nucleus of the BCG in the $H_E$ image. Positive Δ RA are counted westward. The vertical line indicates the radius $a = 12'$ beyond which background inhomogeneities could alter the profiles of the ICL (see Appendix A).

shape of the isophotes in the $I_E$, $Y_E$, $J_E$, and $H_E$ images are well matched quantitatively. Figures 6 and 7 show that the ellipticities, position angles, and centroids of the fitted ellipses to all four images of the BCG+ICL and the iso-density contours of the GC map are similar. The ellipticity increases from $\epsilon = 0$ to $\epsilon = 0.4$ over the inner 100 kpc in both light and GC tracers, whereas the position angles of the ellipses are consistently between −10 and +10 deg. Beyond 100 kpc, the distribution of both the ICL and the ICGCs deviate significantly from a circular profile with an ellipticity of $\epsilon \sim 0.4$.

There is also a close correspondence in the position of the ellipse centroids for the BCG+ICL measured at all four wavelengths. The small differences in centroids can be explained by the remaining background inhomogeneities in the individual images. The spatial distributions of the blue features in Figs. 2b and 2c suggest that inaccurate cirri subtraction may be responsible for the ICL appearing to shift north in the $I_E$ image as well as its slightly rounder shape at $a > 250$ kpc. Overall, the similar contour shapes in the $I_E$ and $H_E$ images validate the reliability of the ellipsoidal fits to the BCG+ICL.

One of the most prominent features in Figs. 4 and 5 is that ICL and ICGC contours on the largest scales ($a \sim 320$ kpc) are not centred on the BCG, but rather are offset westwards of the BCG core. Figure 7 shows that this offset is seen at all wavelengths and in the ICGC distribution – although the western offset is about a factor of two smaller in the ICGCs than the diffuse light. We cannot attribute this offset to incomplete or overzealous cirri subtraction given that this offset is also observed in the distribution of ICGCs, which is not influenced by the presence of cirri.

In summary, we have shown in Figs. 4–7 that the ICL and ICGCs share a coherent spatial distribution. The elliptical contours used to model their distributions have similar ellipticities and position angles for the entire radial range for which they can be measured ($a = 350$ kpc). Such a close correspondence suggests that these two tracers of the intracluster stellar population have a common origin and/or they are well mixed and their distribution is governed by a common potential.

**Table 1.** Directly integrated structural parameters of the BCG+ICL surface brightness profiles within $a < 500$ kpc, including the half-light radius along the semi-major axis, $a_e$, the surface brightness at the half-light radius, $\mu_e$, the total extinction-corrected luminosity within the BCG+ICL measured within the $a = 500$ kpc ellipse in units of solar luminosities, and the fraction of cluster light in the BCG+ICL component, $f_{BCG+ICL}$, measured within the $a = 500$ kpc ellipse.

| Filter | $a_e$ [kpc] | $\mu_e$ [mag arcsec$^{-2}$] | $L_{<500\,kpc}$ [$10^{12}$ L$_\odot$] | $f_{BCG+ICL}$ % |
|---|---|---|---|---|
| $I_E$ | 74 ± 5 | $24.73^{-0.29}_{+0.34}$ | 0.54 ± 0.07 | 31 ± 7 |
| $Y_E$ | 114 ± 4 | $24.59^{-0.15}_{+0.17}$ | 1.14 ± 0.08 | 38 ± 7 |
| $J_E$ | 107 ± 3 | $24.40^{-0.11}_{+0.10}$ | 1.23 ± 0.06 | 32 ± 6 |
| $H_E$ | 96 ± 3 | $24.17^{-0.15}_{+0.10}$ | 1.56 ± 0.07 | 37 ± 6 |

### 5.2. Radial profile of the intracluster light and intracluster globular clusters

We constructed radial surface brightness profiles of the BCG+ICL using the isophotal contours defined using the $I_E$ image and measured the median flux within the annuli in both

**Table 2.** Best-fit parameters of the double-Sérsic fit to the surface brightness profile of the BCG+ICL in $I_E$ and $H_E$, and the GC surface density profiles around NGC 1275+ICGC and the nearby massive elliptical NGC 1272. For each component, $a_e$ and $\mu_e$ list the half-light radius along the semi-major axis and the surface brightness at the half-light radius, respectively. Total luminosities, $L_{tot}$, and luminosities within 500 kpc of the BCG, $L_{<500\,kpc}$, are corrected for extinction. $N_{tot}$ ($N_{<500\,kpc}$) is the total number of selected GCs with $I_E < 26.3$ (and within 500 kpc), after background subtraction. The uncertainties are either the statistical uncertainties of the best-fit Sérsic parameters or, for $L$ and $N$, propagated uncertainties of the best-fit Sérsic parameters using 1000 Monte Carlo realisations.

| Diffuse light | $a_e$ [kpc] | $\mu_e$ [mag arcsec$^{-2}$] | $n$ | $L_{tot}$ [$10^{12}$ L$_\odot$ ] | $L_{<500\,kpc}$ [$10^{12}$ L$_\odot$ ] |
|---|---|---|---|---|---|
| S1 ($I_E$) | 19 ± 4 | 22.6 ± 0.4 | 4.1 ± 0.5 | 0.34 ± 0.06 | 0.31 ± 0.05 |
| S2 ($I_E$) | 191 ± 16 | 26.5 ± 0.1 | 1.2 ± 0.3 | 0.24 ± 0.03 | 0.24 ± 0.03 |
| S1 ($H_E$) | 16 ± 2 | 21.2 ± 0.2 | 3.2 ± 0.3 | 0.57 ± 0.05 | 0.57 ± 0.05 |
| S2 ($H_E$) | 248 ± 18 | 25.7 ± 0.1 | 1.4 ± 0.2 | 1.23 ± 0.12 | 1.00 ± 0.06 |
| **Globular clusters** | | $N_e$ [arcmin$^{-2}$] | | $N_{tot}$ | $N_{<500\,kpc}$ |
| NGC 1275 + ICGCs | 239 ± 16 | 28 ± 4 | 2.1 ± 0.2 | 39 300 ± 1800 | 31 600 ± 600 |
| NGC 1272 | 31 ± 2 | 90 ± 9 | 1.0 ± 0.3 | 2100 ± 170 | 2100 ± 170 |

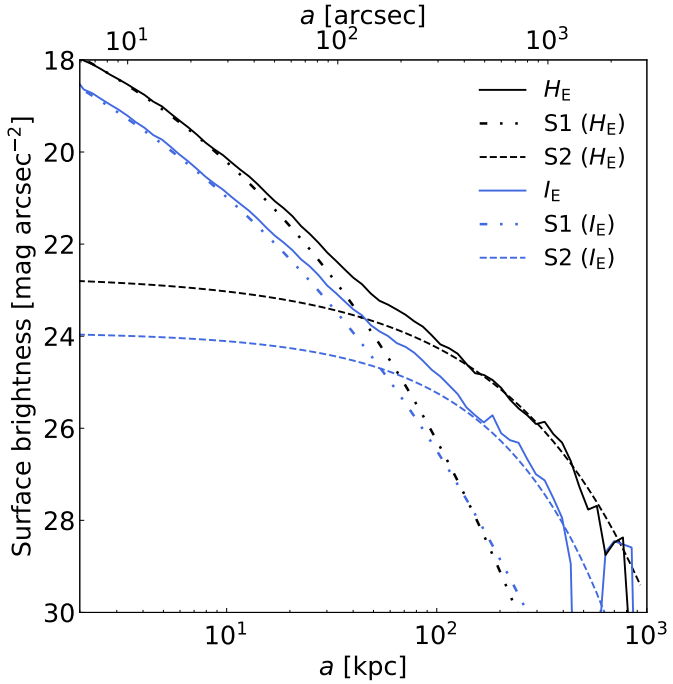


**Fig. 8.** Radial surface brightness profiles of the BCG+ICL in both $I_E$ and $H_E$. The profiles require two Sérsic components to be adequately fit: a compact component (S1) and an extended component (S2). The transition between the profile being dominated by the compact BCG to being dominated by the extended ICL component occurs at $a = 52 \pm 13$ kpc in $I_E$ and $a = 47 \pm 7$ kpc in $H_E$. The radius is not BCG-centric but is given by the semi-major axis radius $a$ of the best-fit ellipse to each isophote with free central coordinates (see Fig. 7).

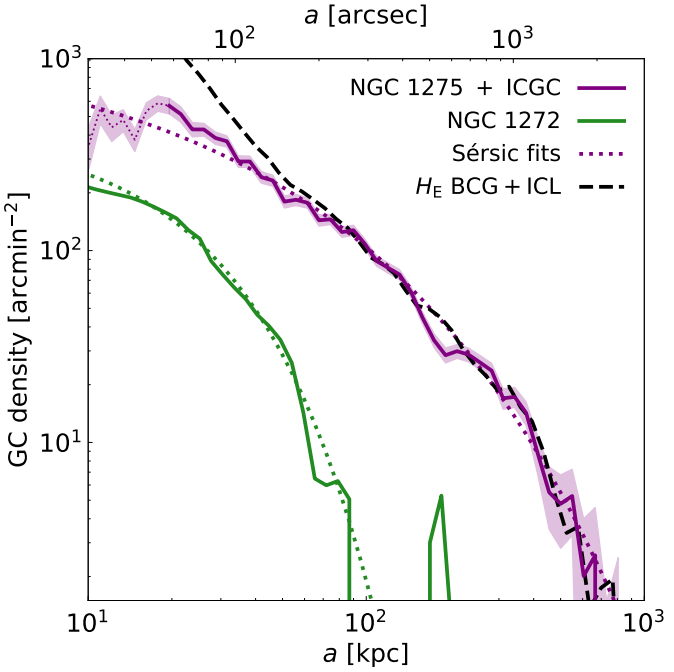


**Fig. 9.** Radial profile of the GC number density surrounding the BCG NGC 1275 (solid purple line) and the nearby galaxy NGC 1272 (solid green line). To construct the profile of NGC 1275, we masked both NGC 1272 and the NGC 1265 (the brightest galaxy in the north of the field-of-view) with ellipses with $a = 100$ kpc. The profile of GCs in both galaxies are well fit by Sérsic profiles (dotted coloured lines), but the GCs associated with NGC 1275 are far more extended, with a measurable excess above the background up to 600 kpc. The radial profile of GCs surrounding NGC 1275 is well matched to the $H_E$- band surface brightness profile of the BCG+ICL (black dashed line, scaled arbitrarily) at radii greater than ~ 50 kpc from the BCG nucleus. A significant fraction of the GCs may be missed in the highly crowded region within 20 kpc of the BCG's core.

$I_E$ and $H_E$ images. These surface brightness profiles are shown in Fig. 8. The ICL is detected above the noise to a distance of ~600 kpc from the BCG in $H_E$, but only ~500 kpc in $I_E$. We show in Appendix A that the $1\sigma$ limiting surface brightness for the 1-D profiles is $\mu(I_E) = 29.4$ mag arcsec$^{-2}$ and $\mu(H_E) = 28.7$ mag arcsec$^{-2}$. These values should not be considered the typical surface brightness limit of ICL detectable in the EWS. On one hand, the exposure time of these ERO is four times that of the EWS, suggesting they should reach fainter depths than the EWS. On the other hand, the EWS avoids bright Galactic cirri and the continuous coverage of the survey area means the background can be more accurately modelled. The detectability of ICL in the EWS will be explored in an upcoming publication (Bellhouse et al. in prep).

Structural parameters obtained by direct integration of the surface brightness and ellipticity profiles within $a < 500$ kpc

are listed in Table 1. Uncertainties were estimated by adding and subtracting the $1\sigma$ background uncertainties (see Appendix A) from the surface flux profiles and integrating the profiles again. The luminosity[4] of the BCG+ICL increases with wavelength from $0.5\times10^{12}$ $L_\odot$ in $I_E$ to $1.6\times10^{12}$ $L_\odot$ in $H_E$. The high concentration of $I_E$ towards the centre of the BCG is likely due to the diffuse blue light from the recent star formation in this galaxy. On the other hand, the concentration ($a_e$) of the BCG+ICL light in the NIR images decreases with wavelength, indicating that the ICL becomes bluer with radius.

We also calculated the fraction of the total cluster light that is emitted from the BCG+ICL. This is defined as $f_{BCG+ICL} = L_{BCG+ICL}/L_{cluster}$, where the luminosity of the cluster includes the satellite galaxies (identified by Cuillandre et al. 2024b and Marleau et al. 2024) within the $a = 500$ kpc isophote ellipse defined in the $I_E$ image. We find that across the four *Euclid* wavebands $f_{BCG+ICL}$ is $\sim$ 35%. The values at each wavelength are given in Table 1, and are consistent with both simulations and observations of other clusters (e.g., Zibetti et al. 2005; Gonzalez et al. 2007; Zhang et al. 2019; Kluge et al. 2021; Sampaio-Santos et al. 2021; Brough et al. 2024).

The BCG+ICL profile in both $I_E$ and $H_E$ requires two Sérsic components to obtain a good fit over most of the radial range: a compact component (labelled S1), and an extended profile (labelled S2). The parameters of both components are listed in Table 2. The transition between light dominated by the S1 component to light dominated by the S2 component occurs at $a = 52 \pm 13$ kpc in $I_E$ and $a = 47 \pm 7$ kpc in $H_E$.

Due to recent star formation occurring in the BCG, the compact S1 component comprises a larger fraction of the BCG+ICL light within 500 kpc at $I_E$ ($56 \pm 11$%) compared to $H_E$ ($36 \pm 4$%). When we extrapolate the BCG+ICL surface brightness profile out to $a = 3.4$ Mpc the amount of light in the S2 component does not increase at $I_E$-wavelengths which tells us that most of the $I_E$ light is limited to within 500 kpc. On the other hand, the S2($H_E$) component increases by 23%, implying that the NIR ICL contributes more at larger radii. When extrapolated to the whole cluster, the extended component (S2) comprises $68 \pm 4$% of the total BCG+ICL $H_E$ light, but we warn that this assumes the outer Sérsic component remains a good fit even though we do not have a measure of the ICL profile beyond 600 kpc.

The GC surface density contours of NGC 1272 and NGC 1275 were fit iteratively, allowing us to separate the GCs of these two giant elliptical galaxies. These galaxies only differ by 1 mag in luminosity, yet the radial distributions of their GCs, plotted in Fig. 9, are remarkably different. Both profiles reveal a flattening towards their cores, consistent with Penny et al. (2012) and Harris & Mulholland (2017), and likely due to incompleteness. However, the central 10–20 kpc region of NGC 1275 contains over twice the GC density of NGC 1272.

The most obvious difference between the profiles of NGC 1275 and NGC 1272 is the extremely wide distribution of GCs around NGC 1275, extending out to 600 kpc. On the other hand, NGC 1272 presents a relatively compact distribution that only extends out to 100 kpc. NGC 1272, which lies 105 kpc west of NGC 1275, contributes negligibly to the GCs within the inner 40 kpc of NGC 1275; however, the ICGCs surrounding NGC 1275 contaminate the GCs in the core of NGC 1272 by up to 25%.

Both the GCs in NGC 1272 and NGC 1275+ICGC can be modelled by a single Sérsic profile, whose parameters are listed in Table 2. NGC 1272 follows an exponential profile, with half the GCs enclosed within 31 kpc of the nucleus, while NGC 1275+ICGCs follow a profile with $n = 2.1 \pm 0.2$, and half of the GCs lie at a distance greater than $239 \pm 16$ kpc, which agrees with the half-light radius for the S2 component in $H_E$ (Table 2). The wide profile of the NGC 1275+ICGCs is remarkably similar to that of the BCG+ICL at radial distances larger than 50 kpc. The $H_E$ BCG+ICL surface brightness profile, shown in Fig. 8, has been arbitrarily normalised and overlaid in Fig. 9 to illustrate the similarity in the radial profiles over the radial range $50 < a/\mathrm{kpc} < 600$.

By directly integrating the structural parameters of the density profiles we find 31 600±600 GCs in the NGC 1275+ICGC within 500 kpc. This is 15 times the number within NGC 1272. Our GC candidates were limited to sources with $I_E < 26.3$, so to extrapolate this measurement to the total number of GCs in the cluster, we must first determine the GC luminosity function (GCLF).

### 5.3. Luminosity function of the globular clusters

We begin by checking whether the GCLF we measure within NGC 1275 matches the expected shape found in previous studies. GCs within giant elliptical galaxies have a luminosity function that follows a Gaussian form (e.g. Jordán et al. 2007). At the distance of Perseus, this Gaussian is expected to peak at a magnitude of $I_E \sim 26.3$ with a $\sigma \sim 1.3$ mag, which is consistent with measurements of NGC 1275 by Harris & Mulholland (2017).

The detection of GCs is a strong function of local surface brightness, with high surface-brightness regions, such as the centre of the BCG, resulting in incompleteness to bright GC magnitudes. Therefore, we start our analysis of the GCLF of NGC 1275 in the elliptical annulus at $20 < a/\mathrm{kpc} \leq 40$, i.e., beyond the bright region within 20 kpc of the nucleus but still within the BCG region where the light from the compact component (S1) dominates over the light from the extended (S2) component (see Fig. 8).

We extended the GC-candidate sample to include all sources with $22.7 < I_E < 28.7$ that match the compactness criteria laid out in Sect. 4.2. This sample of GC candidates contains contamination from background sources, so we measured and subtracted the luminosity function of the background sources. From the radial profile shown in Fig. 9, we detected an excess of GCs out to a semi-major axis of $a = 600$ kpc. We therefore used the region that lies beyond the ellipse with $a = 600$ kpc to select background sources. This background region covers 609 arcmin$^2$, and encompasses 31 911 objects selected by our GC-selection algorithm. We estimate that fewer than 4% of the objects selected in this background region are ICGCs since Fig. 9 shows that the density of GCs beyond this semi-major axis is rapidly decreasing and less than 2 arcmin$^{-2}$.

To estimate the luminosity function of the background sources and its uncertainty, we bootstrapped the sources from the background region 100 times with the sample size limited to the expected number of contaminating sources in the annulus (determined as the annulus area times the surface density of the background region). The luminosity distribution of the background sources is defined as the mean of these 100 realisations, which was then subtracted from the luminosity function derived from the annulus.

The background-subtracted GCLF at $20 < a/\mathrm{kpc} \leq 40$ is shown in red in Fig. 10. The uncertainty is defined as the standard deviation of 100 realisations of the background in each luminosity bin added in quadrature to the Poisson uncertainty of

[4] To transform magnitudes to Solar luminosities, we used the absolute magnitudes of the Sun in the *Euclid* filters given in Appendix C.

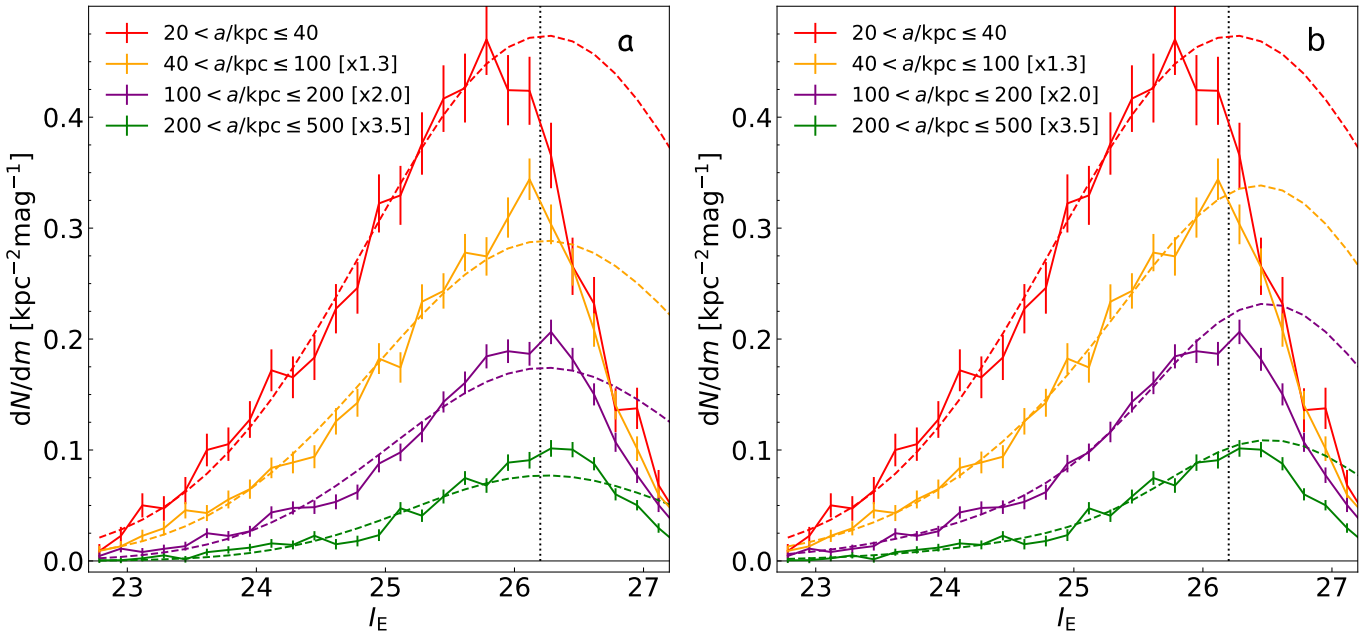


**Fig. 10.** The luminosity function of GC candidates in various elliptical annuli surrounding the BCG. The luminosity function of background sources has been scaled to the area within each annulus and subtracted from each luminosity function. The data have been scaled for clarity according to the numbers shown in the legend. The black dotted line marks the line at which the GC candidate selection is at least 95% complete across the whole image, except in regions of high surface brightness such as the centre of the BCG. In panel a (left), the dashed lines display the single Gaussian that is the best-fit to the luminosity function at $I_E < 26.2$ in each annulus. The best-fit Gaussian parameters are listed in Table 3. In panel b (right), the dashed lines show the 2-component Gaussian distributions that are the best-fit to the luminosity function at $I_E < 26.2$ in the annuli $a > 40$ kpc. The best-fit 2-component Gaussian parameters are listed in Table 4.

**Table 3.** Results of the single Gaussian fits to the GCLF in each annulus. Parameters marked with an asterisk were fixed during the fit. The goodness-of-fit of the model is given by the reduced $\chi^2$ metric.

| Annulus [kpc] | $\mu$ [mag] | $\sigma$ [mag] | reduced $\chi^2$ |
|---|---|---|---|
| 20–40 | $26.24 \pm 0.12$ | $1.39 \pm 0.05$ | 1.01 |
| 40–100 | $26.24^*$ | $1.33 \pm 0.01$ | 1.38 |
| 100–200 | $26.24^*$ | $1.18 \pm 0.02$ | 2.60 |
| 200–500 | $26.24^*$ | $1.05 \pm 0.03$ | 2.28 |

the number of GC candidates in each luminosity bin of the annulus.

We performed a least-squares fit of a Gaussian to this distribution, allowing the mean, amplitude, and width of the Gaussian to be free parameters. The data from this annulus appears to be complete to $I_E = 25.8$ so we limited the fit to $22.7 < I_E < 25.8$. We derived a turn-over magnitude of $I_E = 26.24 \pm 0.12$ and $\sigma = 1.39 \pm 0.05$ mag, which is consistent with empirical expectations (Jordán et al. 2007; Villegas et al. 2010; Harris et al. 2014) and previous measurements of the GCLF within this galaxy (Harris & Mulholland 2017). The goodness-of-fit of the Gaussian model is given by the reduced $\chi^2$ metric. In a fit with 15 degrees of freedom, the reduced $\chi^2$ of 1.01 means the data are consistent with the Gaussian model. Having established that our GC selection and statistical background subtraction are robust, we then measure the GCLF of the intracluster region, which has never been explored to this depth and large radius from the BCG.

We measured the GCLF in three intracluster regions: within annuli of 40 to 100 kpc, 100 to 200 kpc, and 200 to 500 kpc (see Fig. 10). The luminosity function of the background and the errors on the background-subtracted luminosity functions were estimated in the same way as described above. However, we note that our background region is significantly smaller than the 200–500 kpc annulus, which makes the uncertainties on the background in this area unreliable. To account for this, we multiplied our background uncertainty for the 200–500 kpc annulus by 1.56, which is the ratio of the area of the 200–500 kpc annulus to the background region.

We performed a least-squares fit of a Gaussian to these distributions, but the fits did not converge when we allowed the mean, amplitude, and width of the Gaussian to be free parameters. Therefore, we fixed the mean of the Gaussian to be the same as that measured in the 20–40 kpc annulus ($I_E = 26.24$) and solved only for the width and amplitude of the Gaussian. We limited the fitting to the slightly wider range $22.7 < I_E < 26.2$, since the GCs in the intracluster region are complete to fainter magnitudes than the GCs in the BCG, although this does not significantly affect our results.

The best-fit $\sigma$ of the Gaussian distributions range between $1.05 < \sigma/\mathrm{mag} < 1.33$, and although the fits appear reasonable (see Fig. 10a), the reduced $\chi^2$ in Table 3 is high. In each of the fits to the three outer annuli, there are 18 degrees of freedom, so the 95%, 99%, and 99.9% critical values of the $\chi^2$ distribution correspond to a reduced $\chi^2$ of 1.60, 1.93, and 2.35, respectively. Thus the data in the 40–100 kpc annulus is consistent with the Gaussian model, but the model is inconsistent with the data of the 100–200 kpc and 200–500 kpc annuli to > 99% confidence. A further problem with these fits is the significant excess of GCs above the model at magnitudes that are fainter than the completeness limit ($I_E \sim 26.2$). If the models were a good fit to the data, we should only see a deficit of GCs fainter than the completeness limit.

**Table 4.** Results of the double Gaussian fits to the GCLF in the three outer annuli and the single Gaussian fit to the GCLF of the 20–40 kpc annulus. $N_{\rm Tot}$ refers to the total number of GCs in each annulus extrapolated from $I_{\rm E} < 26.2$ assuming the GCLF follows the Gaussian (or double Gaussian) model. The mean of each Gaussian was fixed to the listed $\mu$. $N_2/N_{\rm tot}$ lists the fraction of GCs in the narrow Gaussian component in each annulus. $\sigma_1$ and $\sigma_2$ are the standard deviations of the Gaussian distributions fixed to a mean of $I_{\rm E} = 26.24$ and $I_{\rm E} = 26.54$, respectively. The goodness-of-fit of the model is given by the reduced $\chi^2$ metric having 16 degrees of freedom.

| Annulus [kpc] | $N_{\rm tot}$ | $N_2/N_{\rm tot}$ | $\sigma_1$ [mag] ($\mu_1 \equiv 26.24$) | $\sigma_2$ [mag] ($\mu_2 \equiv 26.54$) | reduced $\chi^2$ |
|---|---|---|---|---|---|
| 20–40 | 6100 ± 400 | – | 1.39 ± 0.05 | – | 1.01 |
| 40–100 | 12 600 ± 800 | 0.25 ± 0.05 | 1.46 ± 0.04 | 0.84 ± 0.07 | 0.93 |
| 100–200 | 17 200 ± 1400 | 0.44 ± 0.08 | 1.48 ± 0.07 | 0.80 ± 0.05 | 1.06 |
| 200–500 | 34 100 ± 2300 | 0.51 ± 0.06 | 1.42 ± 0.07 | 0.72 ± 0.04 | 1.54 |
| 20–500 | 70 000 ± 2800 | 0.40 ± 0.04 | | | |

Since the data are incompatible with a single Gaussian model, we attempted to fit the three outer annuli with a slightly more complex model. We constructed a new model, motivated by observations of the GCLF, consisting of two Gaussian distributions: one with a turn-over magnitude fixed to the BCG value ($I_{\rm E} = 26.24$), and the other fixed[5] to 0.3 mag fainter ($I_{\rm E} = 26.54$), which is the measured turn-over magnitude in dwarf galaxies (Villegas et al. 2010; Carlsten et al. 2022). The widths ($\sigma_1$ and $\sigma_2$) and amplitudes of the Gaussian distributions are allowed to vary[6]. The results of the least-squares fits are shown in Table 4 and Fig. 10b. The fits to the double Gaussian model have 16 degrees of freedom, so the data are consistent with the model in all annuli (i.e. the reduced $\chi^2$ is within the 95% critical value of the $\chi^2$ distribution for all fits).

In all annuli, the standard deviations of the Gaussian fixed to $\mu_{I_{\rm E}} = 26.24$ are very similar ($\sigma_1 \sim 1.44$) and are consistent with the expectation for massive elliptical galaxies. In addition, the standard deviations of the Gaussian fixed to $\mu_{I_{\rm E}} = 26.54$ are also very similar and are consistent with the expectation for dwarf galaxies ($\sigma_2 \sim 0.8$) in all annuli. We reiterate that the annuli were fit independently and, therefore, the similarity in the standard deviations of the best-fit models in each annulus lends credence to the fidelity of our chosen model.

The population of GCs within the narrow GCLF comprises 40 ± 4% of the total GC population in the BCG and intracluster regions. However, there is a strong gradient in the fraction of narrow component to total GCs: 25 ± 5% in the 40–100 kpc annulus, increasing to 51 ± 6% in the 200–500 kpc annulus.

Since background subtraction becomes increasingly important with increasing radius from the BCG, we examined whether the narrow GCLF component may be due to a feature in the derived background luminosity function. If this were the case, we would expect the number of GCs in the narrow GCLF component to increase in proportion to the importance of the background subtraction, which will be proportional to the ratio of the annulus area to the background region area. This ratio is 0.05, 0.19, and 1.56 for the annuli 40–100 kpc, 100–200 kpc, and 200–500 kpc, respectively.

Instead, we find that the number of GCs in the narrow component is $[0.25, 0.70, 1.56] \times 9554$ in the 40–100 kpc, 100–200 kpc, and 200–500 kpc annuli, respectively[7]. There are 3–5 times more narrow-component GCs in the inner annuli than expected if this feature was caused by incorrect background subtraction. We therefore surmise that the GCs in the narrow Gaussian component of the luminosity function are not due to an erroneous feature in the background luminosity function.

Having measured the luminosity function of the GCs, we next corrected our estimates of the total number of GCs for incompleteness. In Table 4, we list the extrapolated number of GCs expected in each elliptical annulus around the BCG and provide uncertainties from the errors on the 2-component Gaussian fit to the luminosity function. In total, we find the BCG+ICGC hosts 70 000 ± 2800 GCs between $20 < a/\mathrm{kpc} \leq 500$. If we conservatively define the intracluster region as the region beyond 100 kpc of the BCG nucleus, then the number of ICGCs is 51 300 ± 2700, which is 73% of this system's total GC population.

### 5.4. Radial colour profile of the BCG+ICL

Radial colour gradients provide valuable constraints on the formation processes of galaxies and, in this case, the BCG and ICL (Zibetti et al. 2005; Montes & Trujillo 2014; DeMaio et al. 2015; Morishita et al. 2017; DeMaio et al. 2018; Contini et al. 2019). Different formation mechanisms are imprinted in the stellar populations of galaxies and, thus, in their radial colour profiles.

The radial colour profiles in $Y_{\rm E} - J_{\rm E}$ and $J_{\rm E} - H_{\rm E}$ have been obtained from the surface brightness profiles that were consistently measured using the BCG+ICL elliptical contours defined using the $I_{\rm E}$ image. Although the BCG+ICL radial surface brightness profiles can be measured up to 600 kpc, the greater uncertainties at large radii mean that colour measurements are unreliable at those radii. Therefore, we limited the colour profiles to the inner 200 kpc. We did not use $I_{\rm E}$ to measure the colours as cirri can strongly contaminate the signal, even after we attempted to subtract it. Cirri were not subtracted from any of the NIR images, but we expect a minimal level of contamination[8] and thus a minimal influence on the BCG+ICL colours.

[5] The model fails to converge if we leave the second turn-over magnitude to be a free parameter.

[6] We also attempted to have both Gaussian distributions centred on $I_{\rm E} = 26.24$, and allowed the widths and amplitudes to vary, but this still left an excess of GCs above the model at magnitudes fainter than the completeness limit.

[7] To obtain these numbers we only counted the number of GCs in the unmasked regions of the annulus, and hence they differ from the numbers quoted in Table 4 for which we interpolated over the masked regions.

[8] The Galactic cirri that contaminate the $I_{\rm E}$ image are not seen as strongly in the NIR (see Fig. 1). This agrees with the modelling of the Galactic cirri in Zhang et al. (2023a), where the scattered light peaks around ~ 7000 Å and drops rapidly at redder wavelengths. *Euclid* will provide key information about the properties of the cirri in the NIR (see also Román et al. 2020).

Figure 11 shows the $Y_E - J_E$ (top panel) and $J_E - H_E$ (bottom panel) radial colour profiles for the BCG+ICL of Perseus. The error in the colour profiles, represented by the shaded regions, is the quadratic sum of the errors in the individual radial surface brightness profiles. We have also plotted the colours of the satellite galaxies of the cluster as measured in Cuillandre et al. (2024b). The hatched area corresponds to radii where there was strong persistence in the individual NISP exposures. Residuals from the imperfectly modelled persistence contaminate this region and therefore the measured colours are not indicative of the true BCG colours. Both colour profiles show two distinct regions: i) a negative gradient up to ∼ 150–270″ (∼ 50–90 kpc), and ii) a region where the colour gradient is almost flat.

To interpret the colour profiles, we assume a constant age for the BCG and ICL. This assuption is justified by studies of nearby clusters show that the age of the ICL is old (≳ 10 Gyr, Williams et al. 2007; Coccato et al. 2010; Gu et al. 2020), and that the expected light-weighted ages are typically between 9 and 13 Gyr (Coccato et al. 2010; Greene et al. 2015; Gu et al. 2020). The colours of such an old stellar population change little within this age range (Bruzual & Charlot 2003; Vazdekis et al. 2016), especially in the NIR colours (as we show in Appendix D).

Under this assumption, the negative colour gradient in region (i) is likely due to negative metallicity gradients: the stellar population of the BCG+ICL becomes more metal-poor towards the outskirts. In region (ii), the colour gradient is approximately flat with a median colour of $Y_E - J_E = 0.05$ and $J_E - H_E = 0.05$. This behaviour is consistent with other BCG+ICL profiles in the literature (e.g., Zibetti et al. 2005; Montes et al. 2014; Spavone et al. 2020; Montes et al. 2021; Golden-Marx et al. 2023; Zhang et al. 2023b). This flattening suggests that the stellar populations in this region are well-mixed, an indication of the accretion of satellites onto the BCG with subsequent virialization of the accreted stars.

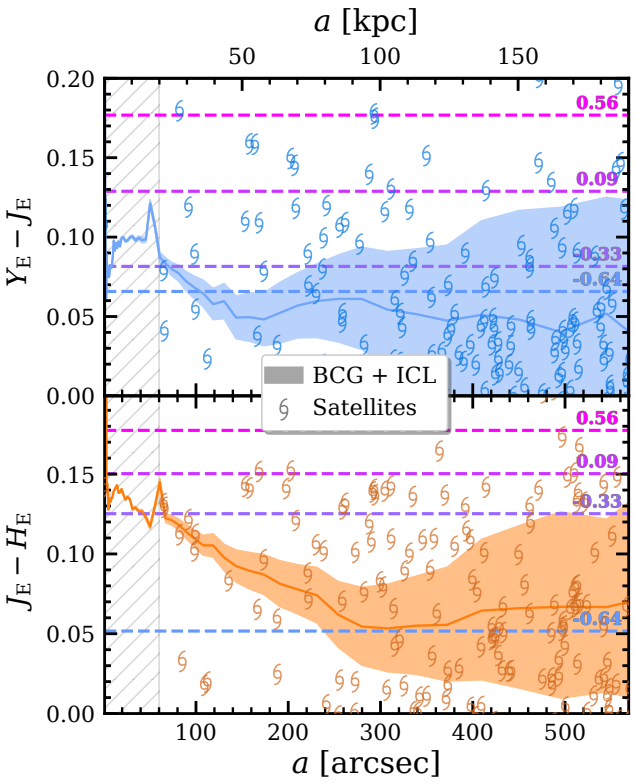


**Fig. 11.** Radial colour profiles of the BCG+ICL. The upper (lower) panel shows the $Y_E - J_E$ ($J_E - H_E$) colour. The colour uncertainties, shown by the shaded areas, are propagated from the uncertainties of the residual background constant in each filter band. The spirals indicate the colours of the satellite galaxies of the cluster as derived in Cuillandre et al. (2024b). The horizontal dashed lines are Bruzual & Charlot (2003) models at a fixed age of 10 Gyr and different [Fe/H] metallicities (as labelled). The hatched area indicates the region with uncertain colours due to persistence residuals.

## 6. Discussion

### 6.1. A new window opens to study the ICL

The results presented here show the extraordinary potential of *Euclid* to observe ICL and ICGCs in nearby galaxy clusters. For the first time, we have mapped the distribution of the ICL and ICGCs in Perseus out to a radius of 600 kpc (∼ $\frac{1}{3}r_{200}$) from the BCG, and measured their properties. Note that the analysis presented here was possible despite the significant Galactic cirri contamination in the field-of-view.

*Euclid* has enabled us to improve these measurements from previous studies in Perseus (Harris & Mulholland 2017; Harris et al. 2020; Kluge et al. 2020) for three main reasons: it has a large field-of-view relative to other optical and NIR space telescopes due to the Korsch three-mirror anastigmat optical design, it is diffraction limited with tight stray light control which yields a compact and highly stable PSF, and it has high spatial resolution in the $I_E$ image which results in a large point source depth.

The large field-of-view enables us to model both bright central galaxies iteratively to identify each galaxy's contribution to the light/GCs in the intracluster region. We have shown that NGC 1272 is relatively compact and only minimally contributes to the diffuse light or GCs in the intracluster region. The large field-of-view also allowed us to map the shape of the GC and ICL distributions out to 350 kpc, which is 150 kpc further than typically achieved using ground-based observations (Kluge et al. 2020; Montes et al. 2021). Previous works on massive clusters at similar distances, (e.g. Peng et al. 2011; Harris et al. 2020) were only able to study the ICGCs in small pockets, constrained by the need to use space-based images to identify GCs, but limited by HST's and JWST's small field-of-view.

While the 0.7 deg$^2$ field-of-view of the *Euclid* ERO enables us to identify intracluster stellar components out to 600 kpc from the BCG, it also limits our analysis as we need to estimate the background from this same field-of-view and the intracluster stellar populations may extend further (see Appendix A). The analysis of galaxy clusters in the EWS (Euclid Collaboration: Scaramella et al. 2022) will not be limited by the field-of-view since that survey will provide nearly continuous coverage of a third of the sky. It will therefore be possible to trace the ICL and ICGCs out to the splashback radius – if they indeed exist out to this distance (Gonzalez et al. 2021; Bellhouse et al. in prep.).

The compact and stable PSF allows us to reliably remove the outer profile of bright stars using only a hundred stars located within the field-of-view. This is most dramatically demonstrated by the bright star that lies between NGC 1275 and NGC 1272 and severely contaminates the ICL in this region.

The detection of the ICGCs is possible only thanks to the large point source depth of *Euclid*, which results from the combination of the compact PSF and high spatial resolution of the VIS instrument that produced the $I_E$ image (see Fig. 3, middle panel). Unfortunately, the undersampling of the PSF for the NIR data prevented us from identifying the NIR counterparts to the $I_E$ sources (see Fig. 3, right panel) and measuring their colours.

While ICGCs have previously been detected in Perseus (Harris & Mulholland 2017; Harris et al. 2020), the *Euclid* ERO have enabled the first assessment of their global distribution. These data allow a direct comparison to the ICL, and quantification of the GCLF as a function of distance from the BCG, which enables the first accurate measure of the total number of ICGCs in this cluster. Euclid Collaboration: Voggel et al. (in prep.) has shown that GCs will be detectable in the EWS in galaxies up to a distance of 100 Mpc ($z \sim 0.023$). Extrapolating using the Yang et al. (2007) group catalogue from the SDSS spectroscopic data release 7, we estimate that there are 90 groups and clusters in the 14 000 deg$^2$ EWS footprint with a total mass greater than $10^{13}$ M$_\odot$ for which we can perform similarly detailed ICGCs studies.

### 6.2. Evidence for a distinct intracluster stellar population

The surface brightness profiles of the BCG+ICL (Fig. 8) are adequately fit by a combination of two Sérsic profiles: one compact Sérsic (S1) and one extended (S2). The outer component, S2, dominates the light profile beyond $a \sim 50$ kpc, where the diffuse light follows the GCs. It is tempting to associate these components with the physical systems of the BCG (S1) and the ICL (S2). This division implies that 44 ± 11% ($I_E$) to 68 ± 4% ($H_E$) of the light of the BCG+ICL system is from the ICL. Vazdekis et al. (2016) show that the stellar mass-to-light ratio, $M/L$, in $H_E$ is approximately 1.0 for a wide range of metallicities. Under these assumptions, 68% of the mass of the BCG+ICL system lies in the ICL.

On the other hand, there has long been a debate as to whether a physically meaningful division can be made between the BCG and the ICL from radial surface brightness profiles alone, and if so, where this division is physically located (e.g., Gonzalez et al. 2005; Dolag et al. 2010; Bender et al. 2015; Remus et al. 2017; Kluge et al. 2021; Contini et al. 2022; Brough et al. 2024). Simulations show that BCGs are made up of as much as 70% of accreted, ex-situ material (e.g., Pillepich et al. 2018), so the BCG and ICL appear to have a similar origin. Therefore separating the components using radial profiles might not be physically meaningful.

While we are reluctant to define a hard boundary between the BCG and ICL components from the radial profiles alone, we have presented further evidence that the BCG and ICL of Perseus should be considered distinct systems of stars, albeit sometimes overlapping.

- We showed that the ICL component is not centred on the BCG, but rather at a point $\Delta$RA $\approx$ 60 kpc west of the BCG (see Fig. 7). This implies the systems of stars that make up the BCG and ICL are not centred at the same location.
- The ellipticity of the BCG+ICL changes with radius. It rises rapidly from the BCG core up to $a = 150$ kpc, and flattens thereafter (Fig. 6). This suggests that the orbital paths of the stars in the BCG and ICL components differ.
- The colour of the BCG+ICL, shown in Fig. 11, gradually becomes bluer until $a = 50$–90 kpc, whereafter the colour is constant (with large uncertainties). This suggests the BCG and ICL comprise of stellar populations with different metallicities.

There is also evidence that the GCs in the BCG are distinct from the ICGCs. We illustrate this through the radial profile of the specific frequency of GCs (defined as the parameter $T$ by Zepf & Ashman 1993). The specific frequency was calculated as the ratio of the GC radial surface density (corrected to account for incompleteness using the GCLFs measured in Sect. 5.3) to the BCG+ICL surface mass density (calculated from the $H_E$ surface brightness profile assuming $M/L = 1.02$ M$_\odot$/L$_\odot$; Vazdekis et al. 2016).

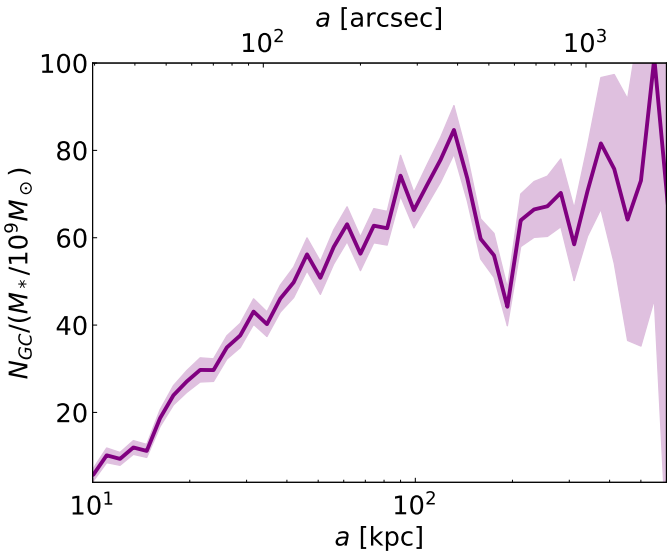


**Fig. 12.** The radial profile of the specific frequency of GCs in NGC 1275+ICGCs, defined as the ratio of GCs to stellar mass in units of $10^9$ M$_\odot$. The specific frequency within the central 10 kpc is consistent with other BCGs, but then increases to a value typically found only in dwarf galaxies or the outskirts of massive galaxies.

In Fig. 12, we show that the specific frequency increases from 10 GCs per $10^9$ M$_\odot$ at 10 kpc to $\sim$ 60 GCs per $10^9$ M$_\odot$ at $a \sim 50$ kpc. The specific frequency of the GCs then remains approximately constant until $a = 600$ kpc. The different specific frequencies implies that the GCs in the inner ($a \lesssim 50$ kpc) and outer ($a \gtrsim 50$ kpc) parts of the BCG and intracluster space trace different stellar populations, and perhaps had different origins.

Catalogues of the specific frequency of GCs are provided by Peng et al. (2008), Liu et al. (2019), and Carlsten et al. (2022), who show that $T = 10$ is consistent with the GC content of galaxies with masses $M > 10^{11}$ M$_\odot$. Larger specific frequencies are associated with dwarf galaxies with $M < 10^9$ M$_\odot$, and are inconsistent with galaxies in the mass range $10^{9.7} < M/\mathrm{M}_\odot < 10^{11}$, which have the lowest values of specific frequency.

The specific frequency of GCs commonly rises with radius in elliptical and S0 galaxies, similar to what we observe at $a < 50$ kpc, as a consequence of the radial profile of light being steeper than the profile of GC number densities (Hargis & Rhode 2014). This is interpreted as evidence that the outskirts of giant ellipticals and S0s were built from the gradual accretion of dwarf galaxies – a process that also leaves radial gradients in the age and metallicity of the stellar population. On the other hand, a constant $T \sim 60$ GCs per $10^9$ M$_\odot$ at $a > 50$ kpc suggests that the ICGCs and ICL at these large radii are well-mixed.

### 6.3. Intracluster stars as tracers of the dark matter halo of Perseus

Recent work by Montes & Trujillo (2019) showed that ICL traces the global distribution of dark matter extremely well for six clusters observed with HST. This sparked a strong interest in using the ICL to study massive dark matter halos. This work has been followed by a plethora of simulations that have confirmed that the global ICL distribution is expected to trace the under-

lying dark matter (Alonso Asensio et al. 2020; Yoo et al. 2022; Contreras-Santos et al. 2024). Confirming this, the ICL has been shown to be a reliable tracer of the position angle of the hosting dark matter halo as well as its spatial offset with respect to the BCG (Kluge et al. 2021).

The shape of the ICL and ICGC distribution in Perseus is consistent with an ellipse of $\epsilon = 0.4$, which agrees with the predictions of triaxial halo ellipticity from $\Lambda$ cold dark matter (Oguri et al. 2010). This ellipticity matches the galaxy distribution but deviates from the large-scale distribution of the intracluster medium traced by X-rays (see Fig. 13) and the Sunyaev-Zeldovich signal in the *Planck* data, which displays a rounder shape. Ettori et al. (1998) finds the X-ray emission has an ellipticity of $\epsilon = 0.06 \pm 0.04$ at $a = 80$ kpc and only $\epsilon = 0.22 \pm 0.07$ at $a = 480$ kpc from the BCG. As a collisionless tracer, the ICL is a more faithful tracer of the dark matter distribution than the collisional X-ray emitting gas (Montes & Trujillo 2019) and is therefore likely to be a better direct tracer of the dark matter halo's ellipticity. The ICL measured in the EWS will provide the ellipticity measurements of many thousands of clusters enabling us to explore the ellipticity distribution of dark matter halos to test dark matter models.

Since light at $H_E$ wavelengths closely traces the stellar mass, we derived the stellar mass density profile for Perseus using Eq. (1) in Montes & Trujillo (2014) assuming a $M/L = 1.02$ (Vazdekis et al. 2016). We measured the slope $\alpha_{2D}$ of the BCG+ICL from 20 kpc to 470 kpc, calculated as $\delta \log \Sigma_* / \delta \log a$, obtaining $-1.47 \pm 0.02$. This value translates into a 3D slope of $\alpha_{3D} \sim -2.47$, using Eq. (5) in Stark (1977), which agrees with measurements of the radial slope of the BCG+ICL stellar mass density in other clusters (Montes & Trujillo 2018, 2022). As shown in Fig. 9, the ICGCs of Perseus also follow this slope (see also Reina-Campos et al. 2023; Kluge et al. 2023).

Pillepich et al. (2014, 2018) found that within high-mass simulated halos, the 3D slope of the stellar halo becomes as shallow as that of the dark matter with $-2.6 < \alpha_{3D} < -2$. This implies that the slopes of both the ICL and the ICGCs measured here are similar to that of the dark matter and they are good luminous tracers of the dark matter in clusters of galaxies. However, we note that we do not know the exact slope of the dark matter halo of Perseus, and studies of other clusters have shown that the slope of the stellar light of clusters can be shallower than the slope of the dark matter (e.g., Diego et al. 2023).

### 6.4. Interpretation of the observed spatial offsets

Characterising the centre of a galaxy cluster is not straightforward. Since the distribution of dark matter can only be inferred indirectly, the exact position of the density peak is unknown. The centre of the dark matter potential well can be estimated using various proxies: the X-ray centroid, the location of the BCG, the centroid of the large-scale dark matter distribution determined using weak gravitational lensing, or the centroids of the ICL and ICGC distributions. While these centroids should be nearly identical in a fully relaxed cluster, recent mergers of either the BCG or the cluster itself may result in offsets.

In Perseus we find disagreement between many of these tracers of the cluster centroid. Fig. 7 highlights a misalignment of $\Delta$RA $\sim 60$ kpc between the BCG and the centroid of the large-scale ICL and ICGCs distributions (especially the isophotes and iso-denisty contours at $a > 200$ kpc), such that the ICL and ICGCs are centred to the west of the BCG.

Recent weak gravitational lensing analysis of the Perseus clutser by HyeongHan et al. (2024) reports a similar westward offset of the total mass distribution from the BCG. They also report a westward mass bridge connecting the BCG to NGC 1264, which lies 430 kpc west of the BCG. On the other hand, Fig. 13 shows that the gaseous intracluster medium, as traced by the isophotes of the X-ray emission, is also offset, but it is offset to the east of the BCG such that there is an even larger offset between the large-scale X-ray emission and the large-scale ICL and ICGC centroids.

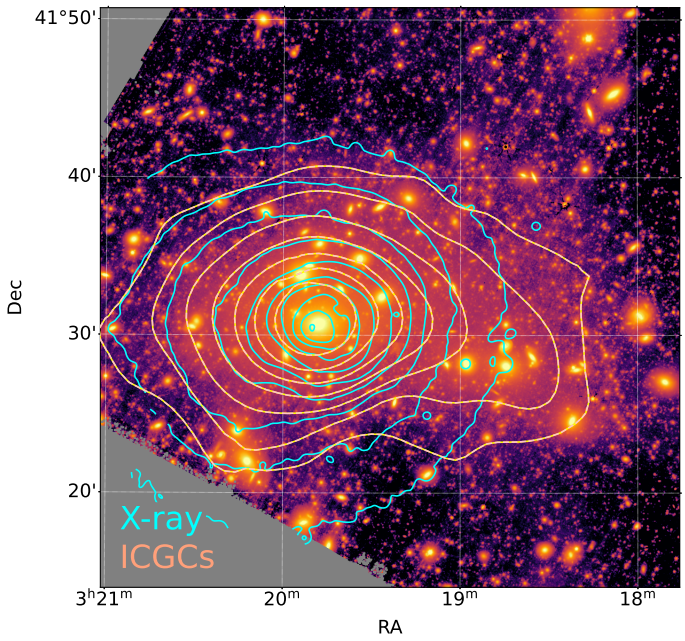


**Fig. 13.** Comparison between the X-ray, the ICL and the ICGCs of Perseus. The background image is the $H_E$ image with the light from NGC 1272 modelled and subtracted. Cyan contours show the X-ray emission of the intracluster medium observed by *Chandra* (Sanders et al. 2016), adaptively smoothed to reach a $S/N = 15$, and further smoothed with a Gaussian kernel of $\sigma = 12''$. Orange contours show the distribution of GCs, not including those from NGC 1272, binned and smoothed with a Gaussian kernel on scales of $40''$.

As clearly shown in Fig. 1, there are 4 – 6 bright galaxies located near the centre of Perseus, and the misalignment of the ICL/ICGCs and the BCG may be due to a superposition of the light and GCs from each of the co-aligned bright galaxies. The main concern is the second brightest galaxy, NGC 1272, which is close in projection to the centroid of the large-scale ICL and ICGC distributions. However, our iterative fitting of the two largest galaxies in the core, NGC 1275 and NGC 1272 (see Sect. 4.3), means that we account for and remove the contribution of NGC 1272 to the light and the GCs in the intracluster region. Figure 13 shows the $H_E$ image after the modelling and removal of the light from NGC 1272, and we can still see the ICL and ICGCs extend to the west. Therefore, the offset between the BCG and the ICL is unlikely to be caused by contamination from NGC 1272.

Perseus is known to be a fairly relaxed cluster (Simionescu et al. 2012), but several studies suggest that Perseus is not completely virialized (Andreon 1994; Churazov et al. 2003) and there are signs that the core is merging with a smaller system (Fabian et al. 2011; HyeongHan et al. 2024). We therefore explore the possibility that the offset of the BCG from the ICL and ICGCs results from this merger activity.

If the merger is ongoing or in its early stages, the observed offset may be the result of ICL and ICGCs associated with the incoming group merging along the merger axis. This would natu-

rally elongate and offset the large-scale ICL and ICGCs towards the direction of the merger, the west. In this scenario, the BCG is representative of the true centroid of the Perseus cluster and the elongation along the merger axis would be a short-term phenomenon that will disappear once violent relaxation settles the ICL and ICGCs into the potential well of the larger Perseus cluster. This model is supported by the models of Churazov et al. (2003) that suggest the sloshing of the X-ray emitting gas is caused by ongoing merging along an east-west aligned filament.

An alternative hypothesis posits that the ICL and ICGCs more accurately trace the distribution of dark matter in the cluster (e.g., Montes & Trujillo 2019) and therefore pinpoints the true cluster centre rather than the BCG. De Propris et al. (2021), and references therein, provide ample evidence for BCG offsets compared to the X-ray defined centroid of clusters, while Kluge et al. (2020) show that offsets between the BCG and the larger-scale ICL are also relatively common.

De Propris et al. (2021) postulate that there are two explanations for the offset: the BCG is moving towards the centre of the halo after being disturbed by a merger, or the dark matter halo is not yet relaxed and oscillates. Harvey et al. (2017) shows that residual wobbling of the BCG can occur long after the merger if the dark matter halo is cored, rather than cuspy (as predicted by standard cold dark matter).

In the case of NGC 1275, we find no evidence for a velocity offset along the line of sight: Aguerri et al. (2020) find that the peak of the velocity distribution of all cluster members is 5258 km s$^{-1}$, which is in good agreement with the velocity of NGC 1275 (5264 km s$^{-1}$, Huchra et al. 1999). Therefore it is unlikely that NGC 1275 is oscillating around or travelling towards the halo centre unless it is moving in the plane of the sky.

The velocity distribution of the dwarf galaxies, however, provides some evidence that the dark matter halo, traced by the ICL and ICGCs, is not yet relaxed and possibly may be oscillating. Marleau et al. (2024) find that the dwarf galaxies in Perseus trace the distribution of the ICL and share a similar centroid as the large-scale ICL and ICGCs. It is therefore possible that the dwarf galaxies, ICGCs, and ICL share the same kinematic distribution as well. Aguerri et al. (2020) find the peak velocity of the Perseus dwarfs is 5049 km s$^{-1}$, i.e., offset by −215 km s$^{-1}$ from the BCG velocity. Therefore, it is plausible that the dark matter halo, traced by the ICL, ICGCs, and the dwarf galaxies, is not yet relaxed after a recent or ongoing merger, and is oscillating around the BCG, which may explain the spatial offset that we observe.

### 6.5. The origin of the stellar populations in the intracluster region

The colours of the ICL and the luminosity function of the ICGCs allow us to infer the mass range of the progenitor galaxies of these stars and, therefore, improve our understanding of how the intracluster stellar component assembled over time. In Sect. 5.4, we presented the radial $Y_E - J_E$ and $J_E - H_E$ colour profiles of the BCG+ICL up to $a = 200$ kpc from the centre of the BCG. From $a = 20$ kpc to $a \sim 60$ kpc, we measure a negative gradient in both colours. Massive elliptical galaxies generally show similar negative gradients in colours (e.g., Peletier et al. 1990; La Barbera et al. 2012; Huang et al. 2018; Santucci et al. 2020), which are interpreted as mostly metallicity gradients due to their formation at high redshift (e.g., Oser et al. 2010; Laporte et al. 2013), especially when exploring their NIR colours (see Appendix D). This interpretation is supported by Penny et al. (2012), whose finding of a blue radial gradient in the colours of the GCs out to 40 kpc also implies a metallicity gradient.

At $a \sim 60$ kpc the colour profiles flatten, and remain constant up to our limit at $a = 200$ kpc. The radius of $a \sim 60$ kpc coincides with the radius beyond which the ICL dominates the surface brightness profiles, and where the $T$ becomes constant (see Fig. 12). Therefore, we interpret this flattening as the consequence of the mixing of the stellar populations of the accreted galaxies that build the ICL and ICGCs.

In Fig. 11 we showed that the ICL has subsolar metallicities ([Fe/H] $\sim -0.6$) at $a > 60$ kpc. This is consistent with ICL metallicities derived for both nearby and intermediate redshift clusters (e.g., Williams et al. 2007; Coccato et al. 2010; Montes & Trujillo 2014, 2018; Gu et al. 2020), and suggests that the progenitors of the ICL are galaxies of a few times $10^9$ M$_\odot$ (using the mass-metallicity relation of Gallazzi et al. 2005). The formation scenario of disrupted dwarf galaxies is also supported by the narrow width of stellar streams in the ICL of the Virgo cluster (Rudick et al. 2010).

On the other hand, the total stellar mass of dwarf galaxies that fall into clusters is too small to account for the large stellar mass of the ICL. Dwarfs can provide less than 10% of the total ICL mass (Martel et al. 2012; DeMaio et al. 2015; Kluge & Bender 2023). This suggests there must be another source of metal-poor stars to populate the ICL. A good candidate is the outskirts of more massive satellites ($\sim 10^{10}$ M$_\odot$) which are easily stripped and exhibit similar metallicities (Pastorello et al. 2014; Greene et al. 2015; Marian et al. 2018).

The properties of the ICGCs provide additional clues to the masses of the progenitor galaxies that contributed to the ICL. Dwarf galaxies ($M < 10^9$ M$_\odot$) have a narrower GCLF ($\sigma \sim$ 0.6–1.0 mag, Villegas et al. 2010) than giant elliptical galaxies ($\sigma = 1.4$ mag) and the peak of the GCLF is ∼0.3 mag fainter for the dwarfs (Jordán et al. 2007; Villegas et al. 2010; Harris et al. 2014).

We find that the GCLF of the BCG, measured in an annulus of $20 < a \leq 40$ kpc matches the GCLF typically found in giant elliptical galaxies (Jordán et al. 2007; Villegas et al. 2010; Harris et al. 2014): the peak of the Gaussian distribution lies at $M_I = -8.1$ mag, with a standard deviation of $\sigma = 1.4$ mag. We conclude that the GCs in this annulus formed in situ within the BCG or in the progenitors of massive elliptical galaxies.

The ICGCs at $a > 100$ kpc are neither consistent with the GCLF of the BCG nor can their GCLF be adequately fit by a single Gaussian. By fitting the data with a more complex model, we find that the GCs at $a > 40$ kpc are better fit by two Gaussian distributions: one of which matches the width of that found in the BCG and is fixed to have the same turn-over magnitude, the other, which is fixed to have a turn-over magnitude that is 0.3 mag fainter, is significantly narrower $\sigma \sim 0.78$ mag. This narrower component is consistent with the GCLF of dwarf galaxies (see above). Therefore the ICGC luminosity function suggests that the progenitor galaxies for these GCs are likely a mix of both giant and dwarf satellite galaxies.

Inferring the progenitors of the ICL from the progenitors of the ICGCs is not straightforward because the specific frequency of GCs is higher for dwarfs with stellar masses $M < 10^9$ M$_\odot$ than for galaxies with intermediate masses $10^{9.7} < M/\mathrm{M}_\odot < 10^{11}$ (see Sect. 6.2). This disproportionately larger GC contribution from dwarfs motivates the simplicity of the two-component GCLF model but we expect a more continuous mass range of ICL progenitors. Nevertheless, we can readily conclude at least some contribution from dwarf galaxies to the ICL at $a > 100$ kpc.

### 6.6. Direct versus indirect accretion of dwarf galaxies

We have shown in Sect. 6.5 that GCs which are consistent with having formed in dwarf satellite galaxies contribute significantly to the ICGCs at $a > 100$ kpc. Given this finding, it is puzzling how dwarfs can be destroyed at large clustercentric distances since the tidal forces of the cluster are too weak to directly disrupt them. The typical effective radius of a dwarf galaxy in Perseus is only 1 kpc (Marleau et al. 2024). Whereas the tidal radius, $r_T \approx D\,(M_{sat}/3M_{cluster})^{1/3}$ (Binney & Tremaine 2008), is large with $r_T = 3.2$ kpc for a typical dwarf galaxy with total mass $M_{sat} = 10^{11}\,M_\odot$ (corresponding to a stellar mass $M = 10^9\,M_\odot$; Wang et al. 2015) in a cluster with a total mass $M_{cluster} = 10^{15}\,M_\odot$, at a clustercentric distance of $D = 100$ kpc, and it increases further with distance.

A possible reconciliation takes into account the high orbit eccentricity of cluster member galaxies (Stark et al. 2019; Aguirre Tagliaferro et al. 2021). On such orbits, the pericentres can reach the central cluster regions where the large tidal forces are sufficient enough to disrupt dwarfs. The liberated stars continue their trajectory and form tidal streams with large apocentres (e.g., Martínez-Delgado et al. 2023). Dynamical friction is inefficient in circularising the orbits of dwarf galaxies, whereas the orbits of massive galaxies are more efficiently circularized by this process (deceleration $dv/dt \propto M_{sat}$, Chandrasekhar 1943). Hence the tidally stripped stars from massive galaxies will reach lower apocentres than those from dwarf galaxies. This procedure can build up gradients in colour, metallicity, age, and GC properties.

Another possibility is an indirect accretion channel. Dwarf galaxies are first accreted onto the outskirts of intermediate-mass galaxies via the procedure described above. These outskirts get subsequently tidally stripped onto the ICL (Bahé et al., in prep.). This process is hierarchical and closely related to the pre-processing formation channel of ICL (Rudick et al. 2006).

Further support for the indirect accretion channel is found in the colours of the GCs in Perseus. While the GCLFs are compatible with a large fraction of the ICGCs originating from massive ellipticals, there is evidence to suggest that these galaxies were not entirely destroyed during ICL and ICGCs assembly. Harris et al. (2020) have shown that 90% of the ICGCs in Perseus are blue and therefore metal-poor. Blue, metal-poor GCs generally dominate dwarf galaxies and the outskirts of massive galaxies, whereas the central regions of massive galaxies are dominated by red (metal-rich) GCs (e.g., Pota et al. 2013). This finding is consistent with GCs from dwarf galaxies being temporarily accreted onto the outskirts of intermediate-mass 'feeder' galaxies that are then tidally stripped and deposited into the intracluster region.

## 7. Conclusions

We present an in-depth analysis of the intracluster stars of the Perseus cluster with the Early Release Observations taken by *Euclid*. To enable analysis of the LSB features we removed contamination by Galactic cirri and large-scale gradients from the $I_E$ image, but no such additional processing was needed for the NIR images. GC candidates were selected as compact point-like sources and we subtracted a background population to derive the distribution and luminosity function of the GCs associated with the cluster.

We detect ICL and ICGCs out to 600 kpc from the BCG, NGC 1275. The BCG+ICL contains a total stellar mass of $1.6 \times 10^{12}\,M_\odot$, making up 35% of the total cluster light within 500 kpc, and there are ~70 000 GCs in this same volume.

The ICL and the ICGCs have a quantitatively similar spatial distribution (Figs. 4 and 5) and follow the same radial slope (beyond 50 kpc; Fig. 9), where we find ~ 60 GCs per $10^9\,M_\odot$ of diffuse light (Fig. 12). The centroid of the isophotes of the BCG+ICL and ICGCs show an increasing offset with radius to the west (decreasing RA), reaching ~ 60 kpc from the centre of the BCG (Fig. 7).

The large-scale distribution of the ICL and ICGCs is qualitatively similar to that of the cluster galaxies, but is inconsistent with the gaseous intracluster medium. The intracluster gas has a lower ellipticity (Fig. 13), and on the largest scales its contours are asymmetric towards the east of the BCG.

This mismatch in the distribution of the cluster components suggests that Perseus is undergoing a merger, but we are not able to distinguish whether the BCG is displaced from the centre of the cluster potential, or the dark matter halo – traced by the ICL and ICGCs – is not relaxed and is oscillating, or if the ICL and the ICGCs from multiple groups are combining along the merger direction and creating the offset.

The isophotes and iso-density contours of the ICL and ICGC distribution have an ellipticity $\epsilon \sim 0.4$, and a radial slope of $\delta \log \Sigma_* / \delta \log a = -2.47$, which is consistent with the expectations of the shape and radial profile of typical cluster-sized dark matter halos. This suggests that these luminous intracluster stellar populations are good tracers of the underlying dark matter.

We present several pieces of evidence that suggest the ICL and ICGCs were predominantly stripped from the low-metallicity outskirts of massive cluster galaxies, with a possible contribution from disrupted dwarf galaxies. The first piece of evidence comes from the NIR colours of the ICL beyond 60 kpc (Fig. 11). We show that the ICL is relatively blue suggesting the stars consist of a low-metallicity population consistent with that of the dwarf galaxies in Perseus or the outskirts of more massive satellite galaxies (~ $10^{10}\,M_\odot$).

Next, we show that the ICL and ICGCs were not assembled from the full destruction of massive cluster galaxies. Most stars and GCs in massive cluster elliptical galaxies are metal-rich and have correspondingly red colours, so the complete destruction of the galaxy would produce a redder ICL than measured. Furthermore, the specific frequency of the GCs in the ICL region is extremely large (60 GCs per $10^9\,M_\odot$ of diffuse light) compared to the typical values found in most galaxies (Liu et al. 2019). If the ICL and ICGCs came from the complete destruction of massive galaxies the specific frequency of the ICGCs would be similar to that of their progenitor galaxies, whereas such high specific frequencies as we observe can be built up by stripping the GC-rich outskirts of massive galaxies.

The ICGCs provide further clues to determine the progenitors of the intracluster stars. First, the two components of the ICGC luminosity function (Fig. 10 and Table 4) imply that ~50% of the ICGCs beyond $a = 100$ kpc belonged to massive cluster satellites at one time. The remaining ~50% have a smaller dispersion in luminosity, consistent with that of dwarf galaxies with stellar masses $\leq 10^9\,M_\odot$. The blue colour of the ICGCs (measured by Harris et al. 2020) supports their origin from low-metallicity progenitors. This can be either dwarf galaxies or the outskirts of intermediate-mass ellipticals. A direct accretion of dwarf galaxies is unlikely because their tidal radius is large at large clustercentric distances. A possible reconciliation is a hierarchical accretion scenario: where dwarf galaxies are accreted onto the outskirts of intermediate-mass 'feeder' galaxies, which are subsequently stripped and deposited into the ICL.

The results presented in this work highlight the power of constraining the stellar assembly history in the intracluster region

by combining a large field-of-view and the resolution required to explore the GC systems of nearby clusters of galaxies. The inclusion of unprecedentedly deep NIR colours in our analysis provides a consistent inference of the progenitor galaxies that make up the ICL and ICGCs.

*Acknowledgements.* NAH and JBGM gratefully acknowledge support from the Leverhulme Trust through a Research Leadership Award, and acknowledge support from the UK Science and Technology Facilities Council (STFC) under grant ST/X000982/1. MM acknowledges support from the Project PCI2021-122072-2B, financed by MICIN/AEI/10.13039/501100011033, and the European Union "NextGenerationEU"/RTRP and IAC project P/302302. TS, AL acknowledge support from Agence Nationale de la Recherche, France, under project ANR-19-CE31-0022. The Euclid Consortium acknowledges the European Space Agency and a number of agencies and institutes that have supported the development of *Euclid*, in particular the Agenzia Spaziale Italiana, the Austrian Forschungsförderungsgesellschaft, funded through BMK, the Belgian Science Policy, the Canadian Euclid Consortium, the Deutsches Zentrum für Luft- und Raumfahrt, the DTU Space and the Niels Bohr Institute in Denmark, the French Centre National d'Etudes Spatiales, the Fundação para a Ciência e a Tecnologia, the Hungarian Academy of Sciences, the Ministerio de Ciencia, Innovación y Universidades, the National Aeronautics and Space Administration, the National Astronomical Observatory of Japan, the Netherlandse Onderzoekschool Voor Astronomie, the Norwegian Space Agency, the Research Council of Finland, the Romanian Space Agency, the State Secretariat for Education, Research, and Innovation (SERI) at the Swiss Space Office (SSO), and the United Kingdom Space Agency. A complete and detailed list is available on the *Euclid* web site (`http://www.euclid-ec.org`). This work has made use of the Early Release Observations (ERO) data from the *Euclid* mission of the European Space Agency (ESA), 2024, https://doi.org/10.57780/esa-qmocze3. This research made use of Photutils, an Astropy package for detection and photometry of astronomical sources (Bradley et al. 2023).

## References

Aguerri, J. A. L., Girardi, M., Agulli, I., et al. 2020, MNRAS, 494, 1681
Aguirre Tagliaferro, T., Biviano, A., De Lucia, G., Munari, E., & Garcia Lambas, D. 2021, A&A, 652, A90
Alamo-Martínez, K. A. & Blakeslee, J. P. 2017, ApJ, 849, 6
Alonso Asensio, I., Dalla Vecchia, C., Bahé, Y. M., Barnes, D. J., & Kay, S. T. 2020, MNRAS, 494, 1859
Andreon, S. 1994, A&A, 284, 801
Bender, R., Kormendy, J., Cornell, M. E., & Fisher, D. B. 2015, ApJ, 807, 56
Binney, J. & Tremaine, S. 2008, Galactic Dynamics: Second Edition
Bradley, L., Sipőcz, B., Robitaille, T., et al. 2023, astropy/photutils: 1.9.0
Brough, S., Ahad, S. L., Bahé, Y. M., et al. 2024, MNRAS, 528, 771
Bruzual, G. & Charlot, S. 2003, MNRAS, 344, 1000
Canning, R. E. A., Fabian, A. C., Johnstone, R. M., et al. 2010, MNRAS, 405, 115
Carlsten, S. G., Greene, J. E., Beaton, R. L., & Greco, J. P. 2022, ApJ, 927, 44
Chandrasekhar, S. 1943, ApJ, 97, 255
Churazov, E., Forman, W., Jones, C., & Böhringer, H. 2003, ApJ, 590, 225
Coccato, L., Gerhard, O., & Arnaboldi, M. 2010, MNRAS, 407, L26
Conselice, C. J., Gallagher, John S., I., & Wyse, R. F. G. 2001, AJ, 122, 2281
Contini, E. 2021, Galaxies, 9, 60
Contini, E., Chen, H. Z., & Gu, Q. 2022, ApJ, 928, 99
Contini, E., Yi, S. K., & Kang, X. 2019, ApJ, 871, 24
Contreras-Santos, A., Knebe, A., Cui, W., et al. 2024, arXiv e-prints, arXiv:2401.08283
Cuillandre, J.-C., Bertin, E., Bolzonella, M., et al. 2024a, A&A, this issue
Cuillandre, J.-C., Bolzonella, M., Boselli, A., et al. 2024b, A&A, this issue
De Propris, R., West, M. J., Andrade-Santos, F., et al. 2021, MNRAS, 500, 310
Deason, A. J., Oman, K. A., Fattahi, A., et al. 2021, MNRAS, 500, 4181
DeMaio, T., Gonzalez, A. H., Zabludoff, A., Zaritsky, D., & Bradač, M. 2015, MNRAS, 448, 1162
DeMaio, T., Gonzalez, A. H., Zabludoff, A., et al. 2018, MNRAS, 474, 3009
Diego, J. M., Pascale, M., Frye, B., et al. 2023, A&A, 679, A159
Dolag, K., Murante, G., & Borgani, S. 2010, MNRAS, 405, 1544
Duc, P.-A., Cuillandre, J.-C., Karabal, E., et al. 2015, MNRAS, 446, 120
Durrell, P. R., Côté, P., Peng, E. W., et al. 2014, ApJ, 794, 103
Edge, A. C., Stewart, G. C., & Fabian, A. C. 1992, MNRAS, 258, 177
Ettori, S., Fabian, A. C., & White, D. A. 1998, MNRAS, 300, 837
Euclid Collaboration: Borlaff, A. S., Gómez-Alvarez, P., Altieri, B., et al. 2022, A&A, 657, A92
Euclid Collaboration: Cropper, M., Al Bahlawan, A., Amiaux, J., et al. 2024, A&A, this issue
Euclid Collaboration: Jahnke, K., Gillard, W., Schirmer, M., et al. 2024, A&A, this issue
Euclid Collaboration: Mellier, Y., Abdurro'uf, Acevedo Barroso, J., Achúcarro, A., et al. 2024, A&A, this issue
Euclid Collaboration: Scaramella, R., Amiaux, J., Mellier, Y., et al. 2022, A&A, 662, A112
Euclid Early Release Observations. 2024, https://doi.org/10.57780/esa-qmocze3
Fabian, A. C., Sanders, J. S., Allen, S. W., et al. 2011, MNRAS, 418, 2154
Feldmeier, J. J., Mihos, J. C., Morrison, H. L., et al. 2004, ApJ, 609, 617
Gallazzi, A., Charlot, S., Brinchmann, J., White, S. D. M., & Tremonti, C. A. 2005, MNRAS, 362, 41
Golden-Marx, J. B., Zhang, Y., Ogando, R. L. C., et al. 2023, MNRAS, 521, 478
Gonzalez, A. H., George, T., Connor, T., et al. 2021, MNRAS, 507, 963
Gonzalez, A. H., Zabludoff, A. I., & Zaritsky, D. 2005, ApJ, 618, 195
Gonzalez, A. H., Zaritsky, D., & Zabludoff, A. I. 2007, ApJ, 666, 147
Gordon, K. D., Clayton, G. C., Decleir, M., et al. 2023, ApJ, 950, 86
Greene, J. E., Janish, R., Ma, C.-P., et al. 2015, ApJ, 807, 11
Gregg, M. D. & West, M. J. 1998, Nature, 396, 549
Gu, M., Conroy, C., Law, D., et al. 2020, ApJ, 894, 32
Hargis, J. R. & Rhode, K. L. 2014, ApJ, 796, 62
Harris, W. E., Brown, R. A., Durrell, P. R., et al. 2020, ApJ, 890, 105
Harris, W. E., Morningstar, W., Gnedin, O. Y., et al. 2014, ApJ, 797, 128
Harris, W. E. & Mulholland, C. J. 2017, ApJ, 839, 102
Hartke, J., Arnaboldi, M., Gerhard, O., et al. 2023, arXiv e-prints, arXiv:2312.02587
Harvey, D., Courbin, F., Kneib, J. P., & McCarthy, I. G. 2017, MNRAS, 472, 1972
Huang, S., Leauthaud, A., Greene, J. E., et al. 2018, MNRAS, 475, 3348
Huchra, J. P., Vogeley, M. S., & Geller, M. J. 1999, ApJS, 121, 287
HyeongHan, K., Jee, M. J., Lee, W., et al. 2024, arXiv e-prints, arXiv:2405.00115
Iodice, E., Capaccioli, M., Grado, A., et al. 2016, ApJ, 820, 42
Jordán, A., McLaughlin, D. E., Côté, P., et al. 2007, ApJS, 171, 101
Kluge, M. 2020, PhD thesis, Ludwig-Maximilians University of Munich, Germany
Kluge, M. & Bender, R. 2023, ApJS, 267, 41
Kluge, M., Bender, R., Riffeser, A., et al. 2021, ApJS, 252, 27
Kluge, M., Neureiter, B., Riffeser, A., et al. 2020, ApJS, 247, 43
Kluge, M., Remus, R.-S., Babyk, I. V., Forbes, D. A., & Dolfi, A. 2023, MNRAS, 521, 4852
La Barbera, F., Ferreras, I., de Carvalho, R. R., et al. 2012, MNRAS, 426, 2300
Laporte, C. F. P., White, S. D. M., Naab, T., & Gao, L. 2013, MNRAS, 435, 901
Laureijs, R., Amiaux, J., Arduini, S., et al. 2011, arXiv:1110.3193
Lee, M. G., Bae, J. H., & Jang, I. S. 2022, ApJ, 940, L19
Liu, Y., Peng, E. W., Jordán, A., et al. 2019, ApJ, 875, 156
Longobardi, A., Arnaboldi, M., Gerhard, O., Pulsoni, C., & Söldner-Rembold, I. 2018, A&A, 620, A111
Marian, V., Ziegler, B., Kuchner, U., & Verdugo, M. 2018, A&A, 617, A34
Marleau, F., Cuillandre, J.-C., Cantiello, M., et al. 2024, A&A, this issue
Martel, H., Barai, P., & Brito, W. 2012, ApJ, 757, 48
Martínez-Delgado, D., Cooper, A. P., Román, J., et al. 2023, A&A, 671, A141
Meisner, A. M. & Finkbeiner, D. P. 2014, ApJ, 781, 5
Mihos, J. C., Harding, P., Feldmeier, J., & Morrison, H. 2005, ApJ, 631, L41
Montes, M. 2022, Nature Astronomy, 6, 308
Montes, M., Brough, S., Owers, M. S., & Santucci, G. 2021, ApJ, 910, 45
Montes, M. & Trujillo, I. 2014, ApJ, 794, 137
Montes, M. & Trujillo, I. 2018, MNRAS, 474, 917
Montes, M. & Trujillo, I. 2019, MNRAS, 482, 2838
Montes, M. & Trujillo, I. 2022, ApJ, 940, L51
Montes, M., Trujillo, I., Prieto, M. A., & Acosta-Pulido, J. A. 2014, MNRAS, 439, 990
Morishita, T., Abramson, L. E., Treu, T., et al. 2017, ApJ, 846, 139
Oguri, M., Takada, M., Okabe, N., & Smith, G. P. 2010, MNRAS, 405, 2215
Oser, L., Ostriker, J. P., Naab, T., Johansson, P. H., & Burkert, A. 2010, ApJ, 725, 2312
Pastorello, N., Forbes, D. A., Foster, C., et al. 2014, MNRAS, 442, 1003
Peletier, R. F., Valentijn, E. A., & Jameson, R. F. 1990, A&A, 233, 62
Peng, E. W., Ferguson, H. C., Goudfrooij, P., et al. 2011, ApJ, 730, 23
Peng, E. W., Jordán, A., Côté, P., et al. 2008, ApJ, 681, 197
Penny, S. J., Forbes, D. A., & Conselice, C. J. 2012, MNRAS, 422, 885
Pillepich, A., Nelson, D., Hernquist, L., et al. 2018, MNRAS, 475, 648
Pillepich, A., Vogelsberger, M., Deason, A., et al. 2014, MNRAS, 444, 237
Planck Collaboration: Abergel, A., Ade, P. A. R., Aghanim, N., et al. 2014, A&A, 571, A11
Planck Collaboration: Aghanim, N., Akrami, Y., Ashdown, M., et al. 2020, A&A, 641, A6
Pota, V., Forbes, D. A., Romanowsky, A. J., et al. 2013, MNRAS, 428, 389
Reina-Campos, M., Trujillo-Gomez, S., Pfeffer, J. L., et al. 2023, MNRAS, 521, 6368

Remus, R.-S., Dolag, K., & Hoffmann, T. L. 2017, Galaxies, 5, 49
Román, J., Trujillo, I., & Montes, M. 2020, A&A, 644, A42
Rudick, C. S., Mihos, J. C., Harding, P., et al. 2010, ApJ, 720, 569
Rudick, C. S., Mihos, J. C., & McBride, C. 2006, ApJ, 648, 936
Sampaio-Santos, H., Zhang, Y., Ogando, R. L. C., et al. 2021, MNRAS, 501, 1300
Sanders, J. S., Fabian, A. C., Russell, H. R., Walker, S. A., & Blundell, K. M. 2016, MNRAS, 460, 1898
Santucci, G., Brough, S., Scott, N., et al. 2020, ApJ, 896, 75
Simionescu, A., Allen, S. W., Mantz, A., et al. 2011, Science, 331, 1576
Simionescu, A., Werner, N., Urban, O., et al. 2012, ApJ, 757, 182
Spavone, M., Iodice, E., van de Ven, G., et al. 2020, A&A, 639, A14
Stark, A., Miller, C. J., & Halenka, V. 2019, ApJ, 874, 33
Stark, A. A. 1977, ApJ, 213, 368
Trujillo, I. & Fliri, J. 2016, ApJ, 823, 123
Tully, R. B., Kourkchi, E., Courtois, H. M., et al. 2023, ApJ, 944, 94
Vazdekis, A., Koleva, M., Ricciardelli, E., Röck, B., & Falcón-Barroso, J. 2016, MNRAS, 463, 3409
Villegas, D., Jordán, A., Peng, E. W., et al. 2010, ApJ, 717, 603
Wang, L., Dutton, A. A., Stinson, G. S., et al. 2015, MNRAS, 454, 83
Williams, B. F., Ciardullo, R., Durrell, P. R., et al. 2007, ApJ, 656, 756
Willmer, C. N. A. 2018, ApJS, 236, 47
Yang, X., Mo, H. J., van den Bosch, F. C., et al. 2007, ApJ, 671, 153
Yoo, J., Ko, J., Sabiu, C. G., et al. 2022, ApJS, 261, 28
Zepf, S. E. & Ashman, K. M. 1993, MNRAS, 264, 611
Zhang, J., Martin, P. G., Cloutier, R., et al. 2023a, ApJ, 948, 4
Zhang, Y., Golden-Marx, J. B., Ogando, R. L. C., et al. 2023b, arXiv e-prints, arXiv:2309.00671
Zhang, Y., Yanny, B., Palmese, A., et al. 2019, ApJ, 874, 165
Zibetti, S., White, S. D. M., Schneider, D. P., & Brinkmann, J. 2005, MNRAS, 358, 949

[1] Max Planck Institute for Extraterrestrial Physics, Giessenbachstr. 1, 85748 Garching, Germany
[2] School of Physics and Astronomy, University of Nottingham, University Park, Nottingham NG7 2RD, UK
[3] Instituto de Astrofísica de Canarias, Calle Vía Láctea s/n, 38204, San Cristóbal de La Laguna, Tenerife, Spain
[4] Departamento de Astrofísica, Universidad de La Laguna, 38206, La Laguna, Tenerife, Spain
[5] Department of Astronomy, University of Florida, Bryant Space Science Center, Gainesville, FL 32611, USA
[6] Université Paris-Saclay, Université Paris Cité, CEA, CNRS, AIM, 91191, Gif-sur-Yvette, France
[7] INAF-Osservatorio di Astrofisica e Scienza dello Spazio di Bologna, Via Piero Gobetti 93/3, 40129 Bologna, Italy
[8] Observatoire Astronomique de Strasbourg (ObAS), Université de Strasbourg - CNRS, UMR 7550, Strasbourg, France
[9] European Space Agency/ESTEC, Keplerlaan 1, 2201 AZ Noordwijk, The Netherlands
[10] Kapteyn Astronomical Institute, University of Groningen, PO Box 800, 9700 AV Groningen, The Netherlands
[11] Max-Planck-Institut für Astronomie, Königstuhl 17, 69117 Heidelberg, Germany
[12] Department of Physics, Université de Montréal, 2900 Edouard Montpetit Blvd, Montréal, Québec H3T 1J4, Canada
[13] Aix-Marseille Université, CNRS, CNES, LAM, Marseille, France
[14] INAF - Osservatorio Astronomico di Cagliari, Via della Scienza 5, 09047 Selargius (CA), Italy
[15] INAF - Osservatorio Astronomico d'Abruzzo, Via Maggini, 64100, Teramo, Italy
[16] Univ. Lille, CNRS, Centrale Lille, UMR 9189 CRIStAL, 59000 Lille, France
[17] Université Paris-Saclay, CNRS, Institut d'astrophysique spatiale, 91405, Orsay, France
[18] Leibniz-Institut für Astrophysik (AIP), An der Sternwarte 16, 14482 Potsdam, Germany
[19] Universität Innsbruck, Institut für Astro- und Teilchenphysik, Technikerstr. 25/8, 6020 Innsbruck, Austria
[20] Université de Strasbourg, CNRS, Observatoire astronomique de Strasbourg, UMR 7550, 67000 Strasbourg, France
[21] Institute of Astronomy, University of Cambridge, Madingley Road, Cambridge CB3 0HA, UK
[22] Waterloo Centre for Astrophysics, University of Waterloo, Waterloo, Ontario N2L 3G1, Canada
[23] Department of Physics and Astronomy, University of Waterloo, Waterloo, Ontario N2L 3G1, Canada
[24] Institute of Physics, Laboratory of Astrophysics, Ecole Polytechnique Fédérale de Lausanne (EPFL), Observatoire de Sauverny, 1290 Versoix, Switzerland
[25] Departamento de Física Teórica, Atómica y Óptica, Universidad de Valladolid, 47011 Valladolid, Spain
[26] Instituto de Astrofísica e Ciências do Espaço, Faculdade de Ciências, Universidade de Lisboa, Tapada da Ajuda, 1349-018 Lisboa, Portugal
[27] INAF-Osservatorio Astronomico di Roma, Via Frascati 33, 00078 Monteporzio Catone, Italy
[28] Observatorio Nacional, Rua General Jose Cristino, 77-Bairro Imperial de Sao Cristovao, Rio de Janeiro, 20921-400, Brazil
[29] Institut d'Astrophysique de Paris, 98bis Boulevard Arago, 75014, Paris, France
[30] OCA, P.H.C Boulevard de l'Observatoire CS 34229, 06304 Nice Cedex 4, France
[31] Instituto de Astrofísica de Andalucía, CSIC, Glorieta de la Astronomía, 18080, Granada, Spain
[32] Université Côte d'Azur, Observatoire de la Côte d'Azur, CNRS, Laboratoire Lagrange, Bd de l'Observatoire, CS 34229, 06304 Nice cedex 4, France
[33] ESAC/ESA, Camino Bajo del Castillo, s/n., Urb. Villafranca del Castillo, 28692 Villanueva de la Cañada, Madrid, Spain
[34] INAF-Osservatorio Astronomico di Brera, Via Brera 28, 20122 Milano, Italy
[35] Dipartimento di Fisica e Astronomia, Università di Bologna, Via Gobetti 93/2, 40129 Bologna, Italy
[36] INFN-Sezione di Bologna, Viale Berti Pichat 6/2, 40127 Bologna, Italy
[37] INAF-Osservatorio Astronomico di Padova, Via dell'Osservatorio 5, 35122 Padova, Italy
[38] Universitäts-Sternwarte München, Fakultät für Physik, Ludwig-Maximilians-Universität München, Scheinerstrasse 1, 81679 München, Germany
[39] INAF-Osservatorio Astrofisico di Torino, Via Osservatorio 20, 10025 Pino Torinese (TO), Italy
[40] Dipartimento di Fisica, Università di Genova, Via Dodecaneso 33, 16146, Genova, Italy
[41] INFN-Sezione di Genova, Via Dodecaneso 33, 16146, Genova, Italy
[42] Department of Physics "E. Pancini", University Federico II, Via Cinthia 6, 80126, Napoli, Italy
[43] INAF-Osservatorio Astronomico di Capodimonte, Via Moiariello 16, 80131 Napoli, Italy
[44] INFN section of Naples, Via Cinthia 6, 80126, Napoli, Italy
[45] Instituto de Astrofísica e Ciências do Espaço, Universidade do Porto, CAUP, Rua das Estrelas, PT4150-762 Porto, Portugal
[46] Faculdade de Ciências da Universidade do Porto, Rua do Campo de Alegre, 4150-007 Porto, Portugal
[47] Dipartimento di Fisica, Università degli Studi di Torino, Via P. Giuria 1, 10125 Torino, Italy
[48] INFN-Sezione di Torino, Via P. Giuria 1, 10125 Torino, Italy
[49] Mullard Space Science Laboratory, University College London, Holmbury St Mary, Dorking, Surrey RH5 6NT, UK
[50] INAF-IASF Milano, Via Alfonso Corti 12, 20133 Milano, Italy
[51] Centro de Investigaciones Energéticas, Medioambientales y Tecnológicas (CIEMAT), Avenida Complutense 40, 28040 Madrid, Spain
[52] Port d'Informació Científica, Campus UAB, C. Albareda s/n, 08193 Bellaterra (Barcelona), Spain
[53] Institute for Theoretical Particle Physics and Cosmology (TTK), RWTH Aachen University, 52056 Aachen, Germany
[54] Dipartimento di Fisica e Astronomia "Augusto Righi" - Alma Mater Studiorum Università di Bologna, Viale Berti Pichat 6/2, 40127 Bologna, Italy

[55] Institute for Astronomy, University of Edinburgh, Royal Observatory, Blackford Hill, Edinburgh EH9 3HJ, UK
[56] Jodrell Bank Centre for Astrophysics, Department of Physics and Astronomy, University of Manchester, Oxford Road, Manchester M13 9PL, UK
[57] European Space Agency/ESRIN, Largo Galileo Galilei 1, 00044 Frascati, Roma, Italy
[58] Université Claude Bernard Lyon 1, CNRS/IN2P3, IP2I Lyon, UMR 5822, Villeurbanne, F-69100, France
[59] UCB Lyon 1, CNRS/IN2P3, IUF, IP2I Lyon, 4 rue Enrico Fermi, 69622 Villeurbanne, France
[60] Departamento de Física, Faculdade de Ciências, Universidade de Lisboa, Edifício C8, Campo Grande, PT1749-016 Lisboa, Portugal
[61] Instituto de Astrofísica e Ciências do Espaço, Faculdade de Ciências, Universidade de Lisboa, Campo Grande, 1749-016 Lisboa, Portugal
[62] Department of Astronomy, University of Geneva, ch. d'Ecogia 16, 1290 Versoix, Switzerland
[63] Department of Physics, Oxford University, Keble Road, Oxford OX1 3RH, UK
[64] INFN-Padova, Via Marzolo 8, 35131 Padova, Italy
[65] INAF-Istituto di Astrofisica e Planetologia Spaziali, via del Fosso del Cavaliere, 100, 00100 Roma, Italy
[66] Institut d'Estudis Espacials de Catalunya (IEEC), Edifici RDIT, Campus UPC, 08860 Castelldefels, Barcelona, Spain
[67] Institut de Ciencies de l'Espai (IEEC-CSIC), Campus UAB, Carrer de Can Magrans, s/n Cerdanyola del Vallés, 08193 Barcelona, Spain
[68] INAF-Osservatorio Astronomico di Trieste, Via G. B. Tiepolo 11, 34143 Trieste, Italy
[69] Aix-Marseille Université, CNRS/IN2P3, CPPM, Marseille, France
[70] Istituto Nazionale di Fisica Nucleare, Sezione di Bologna, Via Irnerio 46, 40126 Bologna, Italy
[71] FRACTAL S.L.N.E., calle Tulipán 2, Portal 13 1A, 28231, Las Rozas de Madrid, Spain
[72] Dipartimento di Fisica "Aldo Pontremoli", Università degli Studi di Milano, Via Celoria 16, 20133 Milano, Italy
[73] Institute of Theoretical Astrophysics, University of Oslo, P.O. Box 1029 Blindern, 0315 Oslo, Norway
[74] Leiden Observatory, Leiden University, Einsteinweg 55, 2333 CC Leiden, The Netherlands
[75] Jet Propulsion Laboratory, California Institute of Technology, 4800 Oak Grove Drive, Pasadena, CA, 91109, USA
[76] Department of Physics, Lancaster University, Lancaster, LA1 4YB, UK
[77] Felix Hormuth Engineering, Goethestr. 17, 69181 Leimen, Germany
[78] Technical University of Denmark, Elektrovej 327, 2800 Kgs. Lyngby, Denmark
[79] Cosmic Dawn Center (DAWN), Denmark
[80] Institut d'Astrophysique de Paris, UMR 7095, CNRS, and Sorbonne Université, 98 bis boulevard Arago, 75014 Paris, France
[81] Department of Physics and Helsinki Institute of Physics, Gustaf Hällströmin katu 2, 00014 University of Helsinki, Finland
[82] Université de Genève, Département de Physique Théorique and Centre for Astroparticle Physics, 24 quai Ernest-Ansermet, CH-1211 Genève 4, Switzerland
[83] Department of Physics, P.O. Box 64, 00014 University of Helsinki, Finland
[84] Helsinki Institute of Physics, Gustaf Hällströmin katu 2, University of Helsinki, Helsinki, Finland
[85] Department of Physics and Astronomy, University College London, Gower Street, London WC1E 6BT, UK
[86] NOVA optical infrared instrumentation group at ASTRON, Oude Hoogeveensedijk 4, 7991PD, Dwingeloo, The Netherlands
[87] Universität Bonn, Argelander-Institut für Astronomie, Auf dem Hügel 71, 53121 Bonn, Germany
[88] Dipartimento di Fisica e Astronomia "Augusto Righi" - Alma Mater Studiorum Università di Bologna, via Piero Gobetti 93/2, 40129 Bologna, Italy
[89] Department of Physics, Centre for Extragalactic Astronomy, Durham University, South Road, DH1 3LE, UK
[90] Université Paris Cité, CNRS, Astroparticule et Cosmologie, 75013 Paris, France
[91] University of Applied Sciences and Arts of Northwestern Switzerland, School of Engineering, 5210 Windisch, Switzerland
[92] IFPU, Institute for Fundamental Physics of the Universe, via Beirut 2, 34151 Trieste, Italy
[93] School of Mathematics and Physics, University of Surrey, Guildford, Surrey, GU2 7XH, UK
[94] School of Mathematics, Statistics and Physics, Newcastle University, Herschel Building, Newcastle-upon-Tyne, NE1 7RU, UK
[95] Department of Physics, Institute for Computational Cosmology, Durham University, South Road, DH1 3LE, UK
[96] Institut de Física d'Altes Energies (IFAE), The Barcelona Institute of Science and Technology, Campus UAB, 08193 Bellaterra (Barcelona), Spain
[97] Department of Physics and Astronomy, University of Aarhus, Ny Munkegade 120, DK-8000 Aarhus C, Denmark
[98] Perimeter Institute for Theoretical Physics, Waterloo, Ontario N2L 2Y5, Canada
[99] Space Science Data Center, Italian Space Agency, via del Politecnico snc, 00133 Roma, Italy
[100] Centre National d'Etudes Spatiales – Centre spatial de Toulouse, 18 avenue Edouard Belin, 31401 Toulouse Cedex 9, France
[101] Institute of Space Science, Str. Atomistilor, nr. 409 Măgurele, Ilfov, 077125, Romania
[102] Dipartimento di Fisica e Astronomia "G. Galilei", Università di Padova, Via Marzolo 8, 35131 Padova, Italy
[103] Departamento de Física, FCFM, Universidad de Chile, Blanco Encalada 2008, Santiago, Chile
[104] INFN-Sezione di Roma, Piazzale Aldo Moro, 2 - c/o Dipartimento di Fisica, Edificio G. Marconi, 00185 Roma, Italy
[105] Satlantis, University Science Park, Sede Bld 48940, Leioa-Bilbao, Spain
[106] Institute of Space Sciences (ICE, CSIC), Campus UAB, Carrer de Can Magrans, s/n, 08193 Barcelona, Spain
[107] Centre for Electronic Imaging, Open University, Walton Hall, Milton Keynes, MK7 6AA, UK
[108] Infrared Processing and Analysis Center, California Institute of Technology, Pasadena, CA 91125, USA
[109] Universidad Politécnica de Cartagena, Departamento de Electrónica y Tecnología de Computadoras, Plaza del Hospital 1, 30202 Cartagena, Spain
[110] Institut de Recherche en Astrophysique et Planétologie (IRAP), Université de Toulouse, CNRS, UPS, CNES, 14 Av. Edouard Belin, 31400 Toulouse, France
[111] INFN-Bologna, Via Irnerio 46, 40126 Bologna, Italy
[112] Dipartimento di Fisica, Università degli studi di Genova, and INFN-Sezione di Genova, via Dodecaneso 33, 16146, Genova, Italy
[113] Centre for Information Technology, University of Groningen, P.O. Box 11044, 9700 CA Groningen, The Netherlands
[114] INAF, Istituto di Radioastronomia, Via Piero Gobetti 101, 40129 Bologna, Italy
[115] Junia, EPA department, 41 Bd Vauban, 59800 Lille, France
[116] Aurora Technology for European Space Agency (ESA), Camino bajo del Castillo, s/n, Urbanizacion Villafranca del Castillo, Villanueva de la Cañada, 28692 Madrid, Spain
[117] Department of Physics and Astronomy, University of British Columbia, Vancouver, BC V6T 1Z1, Canada

## Appendix A: Residual background constant

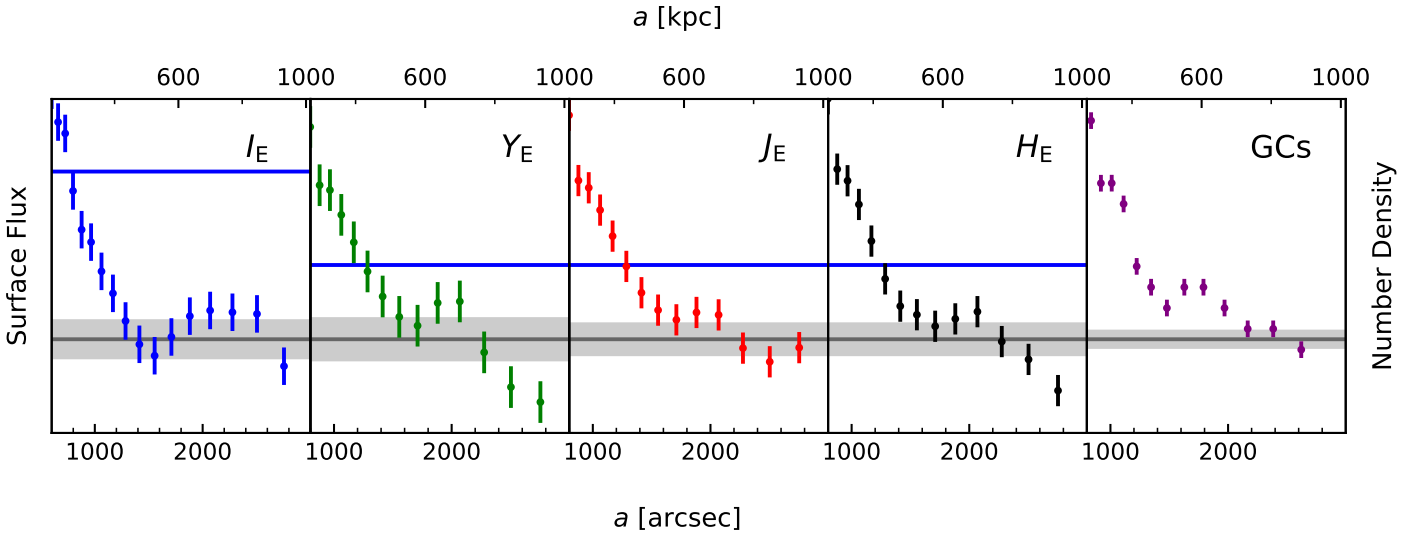


**Fig. A.1.** The residual background constant (dark grey line) is determined for each surface flux profile as the value to which it converges at large radii. The uncertainty is shown by the lighter gray shaded region. The uncertainty of the outer surface flux data points is set to the uncertainty of the background constant. For reference, the blue horizontal line indicates a surface brightness of 27 mag arcsec$^{-2}$.

To calculate surface brightness and number density profiles, we need to first subtract the background. A residual background affecting the stellar light arises from a time-varying background in each detector, Galactic cirri, or scattered light. For the ICGCs, the background contains contamination by background objects and foreground stars that we assume to be distributed homogeneously on large scales.

The background is typically determined as the value to which the surface flux or number density profiles converge at large radii. That value is shown in Fig. A.1 by the darker gray horizontal line. Figure B.1 shows that the background is not perfectly homogeneous. It fluctuates spatially on a level of ~26–27 mag arcsec$^{-2}$. Some of these inhomogeneities average out along the large isophotes shown in the right panels of Fig. B.1. Hence, the outer surface flux profiles in Fig. A.1 contain a significant signal down to more than one magnitude fainter than the blue horizontal line, which indicates a level of 27 mag arcsec$^{-2}$.

Consequently, the uncertainty of the residual background constant is less than the spatial variation visible in the 2-D maps in Fig. B.1. We determine the residual background constants manually as the value to which the surface flux or number density profiles converge. We notice in Fig. A.1 that outermost surface flux data points show trends. This indicates that the scatter in the background is dominated by systematic trends instead of statistical uncertainties. In the $I_E$-band (left panel), the minimum value is reached at $a$ ~1500″ but increases again beyond that. The opposite behaviour is visible in the $Y_E$ and $H_E$ bands. These profiles flatten around $a$ = 2000″ but then continue to decrease further. The $J_E$-band profile and the ICGC profile converge most robustly.

The 1$\sigma$ systematic uncertainties of the residual background constants are also estimated manually, aiming to represent the scatter of the data points in the region where the profile converges. These uncertainties are indicated by the grey shaded regions in Fig. A.1. They correspond to limiting surface brightnesses of $\mu(I_E)$ = 29.4 mag arcsec$^{-2}$, $\mu(Y_E)$ = 28.4 mag arcsec$^{-2}$, $\mu(J_E)$ = 28.7 mag arcsec$^{-2}$, and $\mu(H_E)$ = 28.7 mag arcsec$^{-2}$. We emphasize that these limits may vary when changing from 1-D profiles to 2-D maps or choosing different spatial scales. By estimating both the background constant and its uncertainty, we assign less weight to the data points around $a$ > 2000″ for the stellar light because most of the area along these isophotes is masked and, hence, the surface flux becomes more sensitive to small-scale variations in the background. For the ICGCs, we assign less weight to the outermost data point because of edge effects (see bottom row in Fig. B.1). Finally, the background uncertainty is adopted as the uncertainty in surface flux or number density for the outer data points.

## Appendix B: Masks, Models & Residual Images

The derived ICL distributions are sensitive to the masking of high surface-brightness sources, so we show the masked regions in both Figs. B.1 and B.2.

In Fig. B.1, we show: the original images (with the model for NGC 1272 subtracted; first column), the masked images (second column), the residual images (third column), and the isophote models (fourth column). The residuals are obtained by subtracting the model images from the original images.The first four rows correspond to the filter bands $I_E$, $Y_E$, $J_E$, and $H_E$, while the last row shows the map of the GCs.

The isophotes were fitted to the $I_E$ band image and then also used for the other filter bands to measure the surface fluxes. This is done to obtain colour profiles that are unaffected by the slightly different apparent shapes of the ICL in the different filter bands. The only exception is the ICGCs, for which we used the iso-density contours determined on the ICGC image instead of $I_E$.

The BCG is a complex system with diffuse light emitted from an emission line nebula that extends more than 50 kpc from the nucleus (Conselice et al. 2001). We therefore apply a manual re-masking of NGC 1275 to ensure that we remove the signal from these regions. The result of this manual re-masking is shown in Fig. B.2.

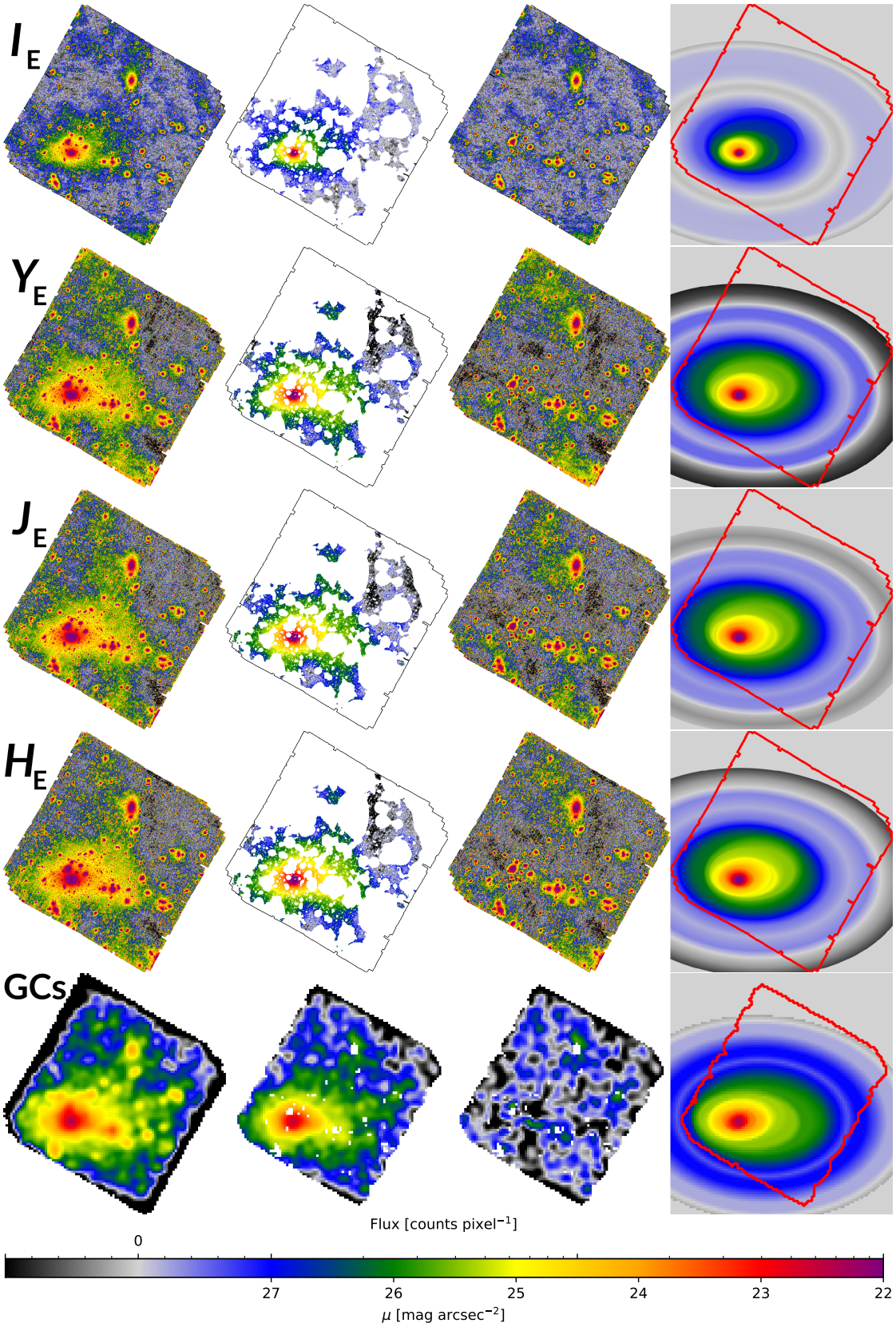


**Fig. B.1.** Original images (first column), masked images (second column), residual images (third column), and isophote models (fourth column). The first four rows correspond to the filter bands $I_E$, $Y_E$, $J_E$, $H_E$, while the last row shows the map of the GCs. The original images have an isophote model for NGC 1272 already subtracted. For the GCs, the mask has been applied to the original image before smoothing. The outlines in columns two and four show the footprint of the images in column one for the integrated light and column two for the GCs.

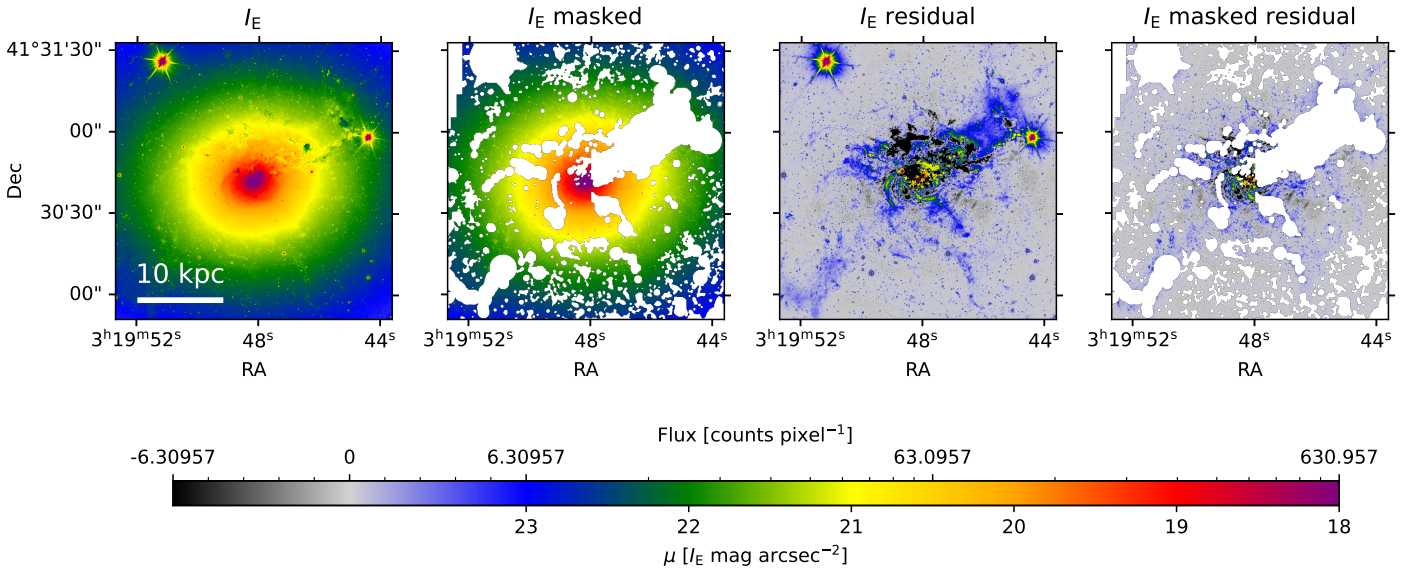


**Fig. B.2.** Zoomed-in region around NGC 1275 visualising the inner masks. North is up and east is left. The original image in the left panel shows star formation and dust towards the north and north-west. These regions are masked in the second panel. The third panel shows the residuals after subtracting the isophote model from NGC 1275. Here, the regions mentioned before plus more filamentary structures in the sound-east and south become readily visible. The masked residual image in the fourth panel shows the accurate masking of these regions.

## Appendix C: Absolute magnitudes of the Sun and absorption in *Euclid* filters for Perseus

**Table C.1.** Absolute AB magnitudes of the Sun in the $I_E$, $Y_E$, $J_E$, and $H_E$ filters, and median Galactic absorption within each filter for the Perseus ERO field-of-view.

| Filter | AB mag | $A_{\rm Filter}$ |
|---|---|---|
| $I_E$ | 4.60 | 0.33 |
| $Y_E$ | 4.54 | 0.17 |
| $J_E$ | 4.58 | 0.11 |
| $H_E$ | 4.78 | 0.07 |

To obtain the absolute magnitudes of the Sun in the *Euclid* filters, we convolved the combined spectrum of the Sun as provided in Willmer (2018), with the filter response curves of the *Euclid* photometric system. The convolution was done following Eq. (1) in Montes et al. (2014).

We also listed the median Galactic absorption within each of the *Euclid* bands for the field-of-view of the Perseus ERO. These are derived using the *Planck* thermal dustmap (Planck Collaboration: Abergel et al. 2014), Gordon et al. (2023) extinction law, and assuming an SED of a 5700 K blackbody. The ICL measurements have been corrected using these median extinctions.

## Appendix D: Stellar population models in the *Euclid* NIR filters

In this section we explore how the *Euclid* NIR colours of stellar populations vary with stellar age. In Fig. D.1 we show the NIR colours of the single stellar population models from Bruzual & Charlot (2003), convolved with the *Euclid* filters following the prescriptions in Montes et al. (2014). The models are colour-coded according to the metallicity, as labelled in the middle panel, and are shown as a function of stellar age. The NIR colours $Y_E - J_E$ and $J_E - H_E$ of the stellar populations show almost no variation with age once the stellar ages are $> 2$ Gyr.

Several studies have shown that the ICL is $\gtrsim 10$ Gyr old (Williams et al. 2007; Coccato et al. 2010; Gu et al. 2020), and therefore, the variation in the NIR colours of the ICL that we observe in Fig. 11 mainly trace a metallicity variation in the stellar population of the ICL.

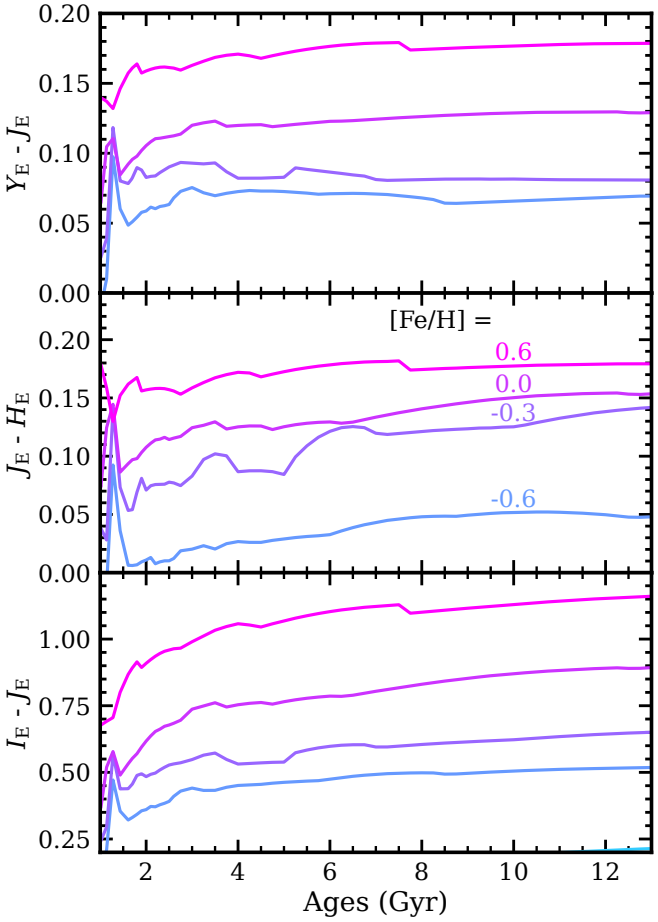


**Fig. D.1.** *Euclid* NIR colours of the Bruzual & Charlot (2003) single stellar population models shown as a function of stellar age. When the stellar population is older than 2 Gyr, its NIR colours, $Y_E - J_E$ and $J_E - H_E$, are fairly constant with age but vary with metallicity.